Taking Optimal Advantage of Fine Spatial Information

Promoting partial image reconstruction for the morphological analysis of very-high-resolution images

**WENZHI LIAO,
JOCELYN CHANUSSOT,
MAURO DALLA MURA,
XIN HUANG, RIK BELLENS,
SIDHARTA GAUTAMA,
AND WILFRIED PHILIPS**

Diverse sensor technologies have allowed us to measure different aspects of objects on Earth's surface [such as spectral characteristics in hyperspectral images and height in light detection and ranging (LiDAR) data] with increasing spectral and spatial resolutions. Remote-sensing images of very high geometrical resolution can provide a precise and detailed representation of the monitored scene. Thus, the spatial information is fundamental for many applications. Morphological profiles (MPs) and attribute profiles (APs) have been widely used to model the spatial information of very-high-resolution (VHR) remote-sensing images. MPs are obtained by computing a sequence of morphological operators based on geodesic reconstruction. However, both morphological operators based on geodesic reconstruction and attribute filters (AFs) are connected filters and, hence, suffer the problem of leakage (i.e., regions related to different structures in the image that happen to be connected by spurious links are considered as a single object). Objects expected to disappear at a given stage remain present when they connect with other objects in the image. Consequently, the attributes of small objects are mixed with their larger connected objects, leading to poor performances on post-applications (e.g., classification).

In this article, we introduce morphological partial reconstruction for spatial-information modeling of VHR urban remote-sensing images. The goal of partial reconstruction is to extract spatial features that better model the attributes of different objects, leading to improved classification performances. These methods are applied to three data sets with different sensor modalities, resolutions, and properties (including panchromatic, hyperspectral, and LiDAR images), and their effectiveness and robustness are quantitatively

and qualitatively evaluated. In addition, the morphological partial reconstruction codes introduced in this article have been implemented in a MATLAB toolbox (http://telin.ugent.be/~wliao/Partial_Reconstruction) that has been made available to the community.

MORPHOLOGICAL PARTIAL RECONSTRUCTION

Recent advances in remote-sensing technology have led to the increased availability of a multitude of satellite and airborne data sources with further enhanced resolution. The term *resolution* refers to spatial, spectral, and temporal resolution. Additionally, at lower altitudes, airplanes and unmanned aerial vehicles can deliver VHR data from targeted locations. Remote-sensing acquisitions employ passive (optical and thermal range and multispectral and hyperspectral) and active devices such as synthetic aperture radar (SAR) and LiDAR. Diverse information of Earth's surface can be obtained from these multiple-imaging modalities. Optical and SAR systems map different properties of the terrain, LiDAR provides the elevation, while multispectral and hyperspectral sensors reveal the material composition.

Despite the richness of information and the increasing resolutions, the automatic interpretation of remote-sensing images remains a challenge [1]–[3]. Raw remote-sensing data have some limitations in producing precise classifications of complex scenes such as urban areas. For example, spectral and/or elevation characteristics of urban land-use classes such as road surfaces, parking lots, and open areas are so similar that they cannot be separated by using either raw spectral images or raw LiDAR data. Consequently, there is an increased interest in developing advanced image-processing algorithms to incorporate spatial information for reliable image classification.

Automated spatial-information extraction employs either object-based or pixel-based approaches. Object-based methods first group the image pixels in a meaningful way via image segmentation [4]. This approach provides a natural means to incorporate geometrical information by calculating the different shape characteristics of the segmented objects. However, the segmentation process typically relies on parameters that are highly dependent on the image data at hand and on the specific tasks [5], [6]. Pixel-based contextual approaches often employ mathematical morphology [7] ranging from low-level feature extraction (FE) (for size and shape features) using MPs [8]–[10] over midlevel APs [11], [12] to high-level FE with semantic

©ISTOCKPHOTO.COM/FILIPEFRAZAO

information indexes [13]–[15]. Recent works demonstrate the benefits of using mathematical morphology in modeling and extracting geometrical information from remote-sensing images for change detection [16]; urban planning [10], [12], [15]; forest management [17]; and risk assessments [18]. The applications of mathematical morphology are of interest well beyond remote sensing for various applications of image processing [27]–[29] and computer vision [30], wherever the interpretation and analysis of VHR images/video is of interest.

Pesaresi and Benediktsson [8] built an MP of an image applying a sequence of opening and closing by reconstruction operators [7] using a structural element (SE) of predefined and increasing sizes. The approach of [9] extended the method in [8] for hyperspectral data with high spatial resolution. The resulting method built the MPs on the first principal components (PCs) extracted from a hyperspectral image, leading to the definition of the extended MP (EMP). Bellens et al. [10] proposed two MPs using disk-shaped and linear SEs to model the width and length of the objects in the VHR panchromatic urban imagery. MPs have been widely applied to the analysis of VHR images, from spatial-characteristics modeling of panchromatic and multi/hyperspectral images [8]–[10] to height information extraction of LiDAR data [2], [17], [19], [20] and amplitude and phase exploitation of SAR [21]–[23]. The efficiency of using MPs to extract additional features for applications (e.g., classification and target detection) has been reported in many recent works [24]–[26].

While MPs are appealing due to their efficiency in extracting spatial information from VHR remote-sensing imagery, they have some limitations when it comes to modeling other geometrical features (e.g., textures). Additionally, SEs are greatly constrained when modeling concepts of the different characteristics of the spatial information (e.g., size, shape, and homogeneity). Recently, Dalla Mura et al. [11] proposed morphological APs for reducing the limitations of the MPs. The APs are obtained by applying a sequence of AFs to a gray-level image [11]. The AFs are operators defined in the mathematical morphology framework that merge connected components at different levels in the image per some measure computed on the components (i.e., attributes) [7]. The APs can be used to extract features that are not only related to the scale of the regions in the image but also relate to any measures (e.g., geometrical, textural, and spectral) that can be computed on the regions. The advantages of APs over MPs have been reported in the literature, including

> **THE APs CAN BE USED TO EXTRACT FEATURES THAT ARE NOT ONLY RELATED TO THE SCALE OF THE REGIONS IN THE IMAGE BUT ALSO RELATE TO ANY MEASURES (E.G., GEOMETRICAL, TEXTURAL, AND SPECTRAL) THAT CAN BE COMPUTED ON THE REGIONS.**
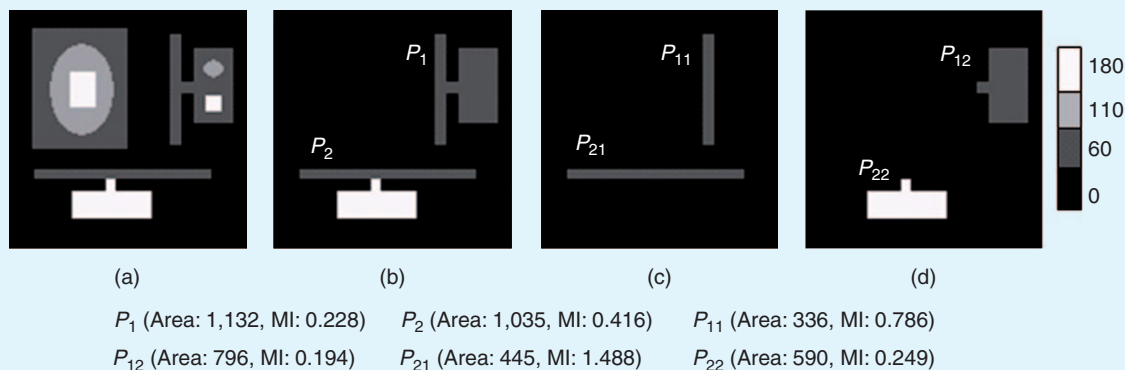
the advantage that APs allow more geometrical features to be modeled for the analysis of VHR images [11], [12], [26], [31], [32]. Applications to multimodal remote-sensing images have recently been reported in [31]–[44].

However, being connected filters, AFs [46]–[48], together with operators based on geodesic reconstruction [7], [49], [50], suffer the problem of leakage [47] (i.e., regions related to different semantic objects in the image happen to be connected by spurious links and so are considered to be a single region), which [10] also refers to as *over-reconstruction problems*. This phenomenon might lead to some unexpected results for remote-sensing images. For example, the size of objects is not accurately estimated when these objects are spatially connected with others in the image. In general, smaller objects are wrongly assigned the attributes of the larger objects connected to them. This is a significant problem for automated content analysis because, in typical remote-sensing scenes, many objects are arranged in a complex manner, i.e., roads are connected to many other objects such as parking lots and buildings. These connected objects are often wrongly treated as a single object by using the connected filters (e.g., AFs [11] and geodesic reconstruction [7]). The situation is even worse for images with noise that might connect two adjacent but nonconnected regions. Clearly, this leads to poor classification performances [51].

To overcome the limitation of over-reconstruction (i.e., the leakage problem) [11], [50], Ronse [45] defined contraction-based connectivity where one can split path-connected components into multiple fragments by cutting them at these spurious links between wider regions. A second-generation connected operator [46] employs a single mask image to shape the connected components, both those bounded by the mask and those outside of it. However, the second-generation connectivity opening with a mask given by an opening or an erosion of the original distorts the edges of an object, as analyzed in [52]. Later, Ouzounis and Wilkinson [52] improved the second-generation connected operator by using an image partition instead of a single mask. Their proposed π-connectivity allows more flexibility than mask-based second-generation connectivity. The approach of [10] proposed a partial reconstruction for morphological opening and closing, where one reconstructs a pixel (of an object) with limited iterations (and not until stability). In our recent work [51], we proposed a partial reconstruction for AFs to better model and extract more geometrical information (including size and shape information) for classifying hyperspectral images. The main characteristic of the partial reconstruction is that it does not wrongly connect objects that should remain disconnected, thus better modeling the spatial information of objects in an image. In addition, with partial reconstruction, the generated profiles contain a smaller amount of redundant information, because the connected objects disappear when the image is progressively simplified. The effective performances of

P_1 (Area: 1,132, MI: 0.228) P_2 (Area: 1,035, MI: 0.416) P_{11} (Area: 336, MI: 0.786)
P_{12} (Area: 796, MI: 0.194) P_{21} (Area: 445, MI: 1.488) P_{22} (Area: 590, MI: 0.249)

FIGURE 1. An example of some connected objects and their attributes in a synthetic image: (a) the input image, (b) connected objects with the same gray level (P_1) and a different gray level (P_2), and (c) and (d) their divisions. MI: moment of inertia.

using morphological partial reconstruction to extract additional spatial information for the analysis of VHR images can be found in our recent work [2], [10], [20], [34], [51], [53], [54].

The main objective of this article is to introduce morphological partial reconstruction for the analysis of VHR images and their applications in the modeling of spatial information from different urban remote-sensing images for classification. In addition, a MATLAB application that implements the morphological partial reconstruction is available, which can be applicable to other disciplines that need efficient methods for analyzing VHR images.

DATA SETS

Four images are used in this article: one synthetic image and three real high-spatial-resolution remote-sensing images. The synthetic image, shown in Figure 1, simulates the real situations in typical remote-sensing scenes, where many objects are arranged in a complex manner, i.e., roads are connected to many other objects such as parking lots (with the same gray level) and buildings (with a different gray level). The main objective of this image is to illustrate the performances of morphological and attribute operators with partial reconstruction to manage such connected objects. The second image is the real high-resolution panchromatic image captured by the IKONOS satellite sensor in a Ghent (Belgium) neighborhood. The third image is a hyperspectral data set of the University of Pavia, Italy, acquired with the Reflective Optics System Imaging Spectrometer (ROSIS-03) optical sensor with 115 spectral bands in the wavelength range from 0.43 to 0.86 μm and a very fine spatial resolution of 1.3 m by pixel. The fourth image is the LiDAR-derived digital-surface model acquired by the National Center for Airborne Laser Mapping (NCALM) over the University of Houston campus and its neighboring area.

1) *Ghent Watersportbaan*: The panchromatic image was acquired on 5 August 2003 of the Watersportbaan in the

city of Ghent, Belgium, with a spatial resolution of 1 m. The remote-sensing scene, consisting of the full 500 × 700 pixels, had nine classes. Figure 2 shows the image and its ground truth.

2) *University of Pavia*: The hyperspectral image with 610 × 340 pixels was collected over the University of Pavia, Italy, with the ROSIS-03. It contains 103 spectral channels after the removal of noisy bands. The data also include nine land cover/use classes. Figure 3 presents false color images and their ground truth.

3) *University of Houston*: The LiDAR image was acquired by NCALM in June 2012 over the University of Houston campus and the neighboring urban area with a spatial resolution of 2.5 m. The whole scene of the data, consisting of the full 349 × 1905 pixels, contains 15 classes. The LiDAR image and

> **THE MAIN CHARACTERISTIC OF THE PARTIAL RECONSTRUCTION IS THAT IT DOES NOT WRONGLY CONNECT OBJECTS THAT SHOULD REMAIN DISCONNECTED.**
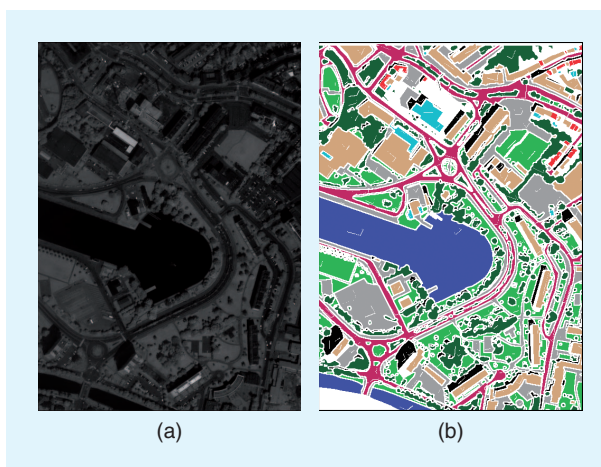

FIGURE 2. The Ghent Watersportbaan image: (a) the panchromatic image and (b) ground truth.
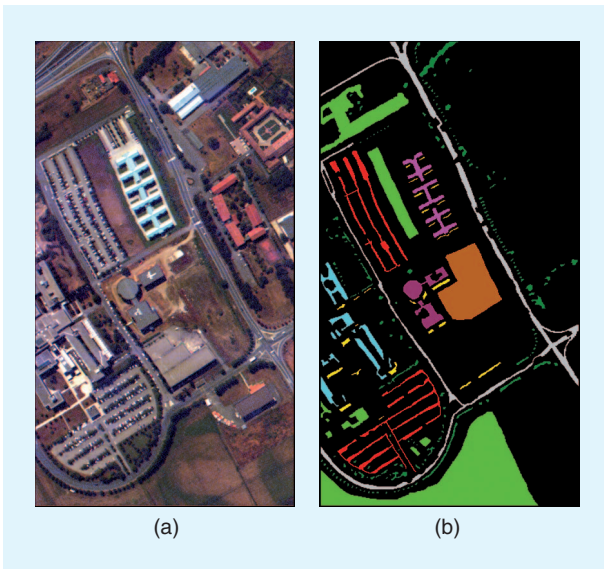
FIGURE 3. The University of Pavia hyperspectral image: (a) LiDAR data and (b) ground truth.
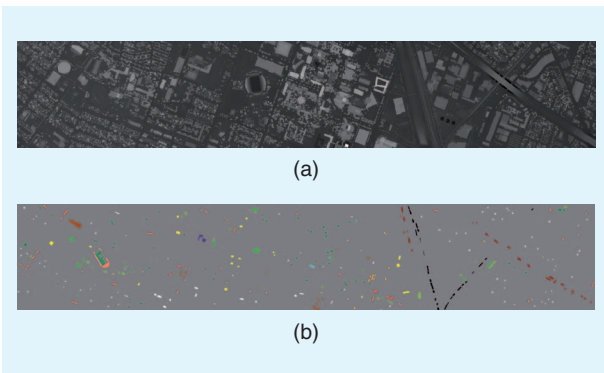

FIGURE 4. The University of Houston image: (a) LiDAR data and (b) ground truth.

its ground truth are shown in Figure 4. For more information, see [2] and [55].

The training and test sets for each data set (shown in Tables 1 and 2) are pixels selected from the data provided by experts who are knowledgeable about the corresponding predefined species/classes. Note that the color in the cell denotes different classes in the classification maps. Pixels from the training set were excluded from the test set in each case and vice versa.

MORPHOLOGICAL FEATURES GENERATED BY CONNECTED FILTERS

Mathematical morphology [7], [49], [50] is a popular tool in image and video processing and has been widely used in diverse tasks such as FE, segmentation, and restoration. Successful applications of mathematical morphology in remote sensing image processing have been reported in [12], [24]–[26], [31]–[34], [36], and [37]. Morphological operators [7] and AFs [11] are two of the most widely used operators of mathematical morphology in remote sensing image processing.

Morphological operators act on the values of the pixels according to transformations that consider the pixels' neighborhood (with a given size and shape). The basic operators are dilation and erosion [7]. These operators are applied to an image with a set of known shapes referred to as the *SEs*. In the case of erosion, a pixel takes the minimum value of all the pixels in its neighborhood defined by the SE. By contrast, dilation takes the maximum value of all the pixels in its neighborhood. Dilation and erosion are usually employed in tandem, either with the dilation of an image followed by erosion of the dilated result or with erosion of an image followed by the dilation of the eroded result. These combinations are known as *morphological opening and closing.*

AFs, such as attribute openings and closings [11], are connected operators, defined in the mathematical morphology framework, that process an image by merging its connected components at different gray levels. Connected components are the flat zones where the image-constant intensity is continuous. An opening acts on bright objects (for LiDAR data, the bright regions are areas with high elevation such as the top of a roof) compared with their surroundings; closings, on the other hand, act on dark (low height in the LiDAR data) objects [2]. For example, an opening merges bright objects that are smaller than the threshold into their background, while the dark objects are left unchanged. The opposite operation of the opening is the closing, which removes small, dark objects while leaving bright objects unchanged. Morphological features are typically generated by applying a sequence of morphological operators or AFs on an image, where MPs contain low-level features (size and shape information) and APs can model middle-level features (e.g., homogeneity and textures).

MORPHOLOGICAL OPERATORS BY RECONSTRUCTION

By increasing the size of the SE, more and more objects are removed, as shown in Figures 5–7. However, aside from deleting objects smaller than the SE, classical morphological openings and closings degrade borders and deform the shapes of the objects, as shown in Figures 5(a), 6(a), and 7(a), and round the corners of rectangular objects. To preserve the shapes of objects, morphological openings and closings by reconstruction (i.e., geodesic reconstruction [49], [50]) are generally the tools of choice [56], [57]. With geodesic reconstruction, the whole object is reconstructed if at least one pixel of the object survives the opening or closing. Two pixels are considered to belong to the same object if they are connected in the original image (or mask). The image on which the reconstruction is performed is called the *marker.* The geodesic dilation (of size 1) of the gray-scale marker image *f* and the mask image *g* is defined as

$$\delta_g^1(f) = \delta^1(f) \wedge g, \tag{1}$$

**TABLE 1. INFORMATION CLASSES AND TRAINING-TEST SAMPLES
FOR THE GHENT WATERSPORTBAAN AND THE UNIVERSITY OF PAVIA.**

GHENT WATERSPORTBAAN			UNIVERSITY OF PAVIA		
CLASS NAME	NUMBER OF TRAINING SETS	NUMBER OF TEST SETS	CLASS NAME	NUMBER OF TRAINING SETS	NUMBER OF TEST SETS
Water	255	34,696	Asphalt	548	6,641
Grass	278	34,484	Meadows	540	18,649
Trees	232	40,516	Gravel	392	2,099
Dark roof	303	32,899	Trees	524	3,064
Red roof	177	1,331	Metal sheets	265	1,345
White roof	190	2,678	Soil	532	5,029
Road	266	27,679	Bitumen	375	1,330
Other man-made	350	40,532	Bricks	514	3,682
Shadows	213	10,013	Shadows	231	947

TABLE 2. INFORMATION CLASSES AND TRAINING-TEST SAMPLES FOR THE UNIVERSITY OF HOUSTON.

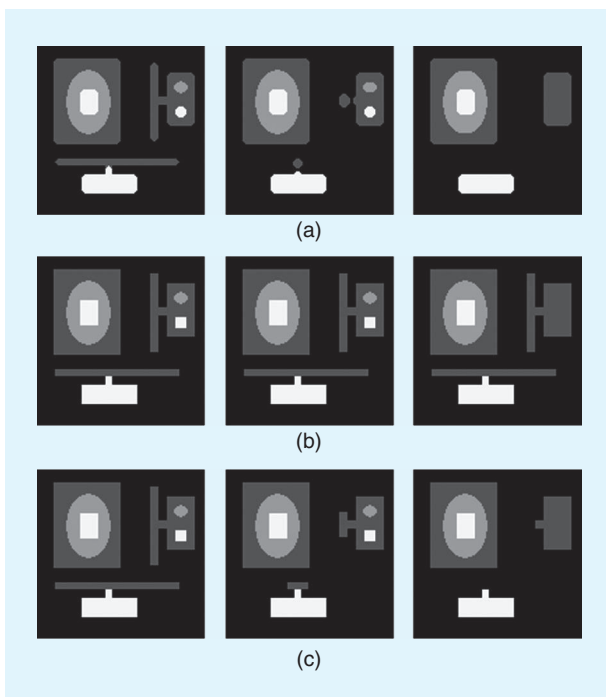| CLASS NAME	NUMBER OF TRAINING SETS	NUMBER OF TEST SETS	CLASS NAME	NUMBER OF TRAINING SETS	NUMBER OF TEST SETS	CLASS NAME	NUMBER OF TRAINING SETS	NUMBER OF TEST SETS
Grass healthy	198	1,053	Grass stressed	190	1,064	Grass synthetis	192	505
Tree	188	1,056	Soil	186	1,056	Water	182	143
Residential	196	1,072	Commercial	191	1,053	Road	193	1,059
Highway	191	1,036	Railway	181	1,054	Parking lot 1	192	1,041
Parking lot 2	184	285	Tennis court	181	247	Running track	187	473

FIGURE 5. The openings with an increasing SE size on a synthetic image. The scales of the SEs vary from two to six with a step increment of two. (a) Without reconstruction, (b) geodesic reconstruction, and (c) partial reconstruction.
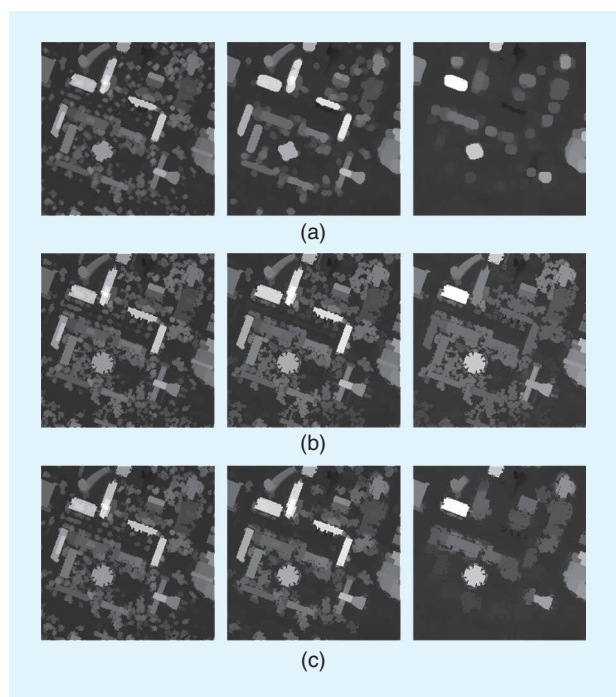

FIGURE 6. The openings with an increasing SE size on the University of Houston LiDAR data (part of the result). The scales of the SEs vary from two to six pixels with a step increment of two pixels. (a) Without reconstruction, (b) geodesic reconstruction, and (c) partial reconstruction.
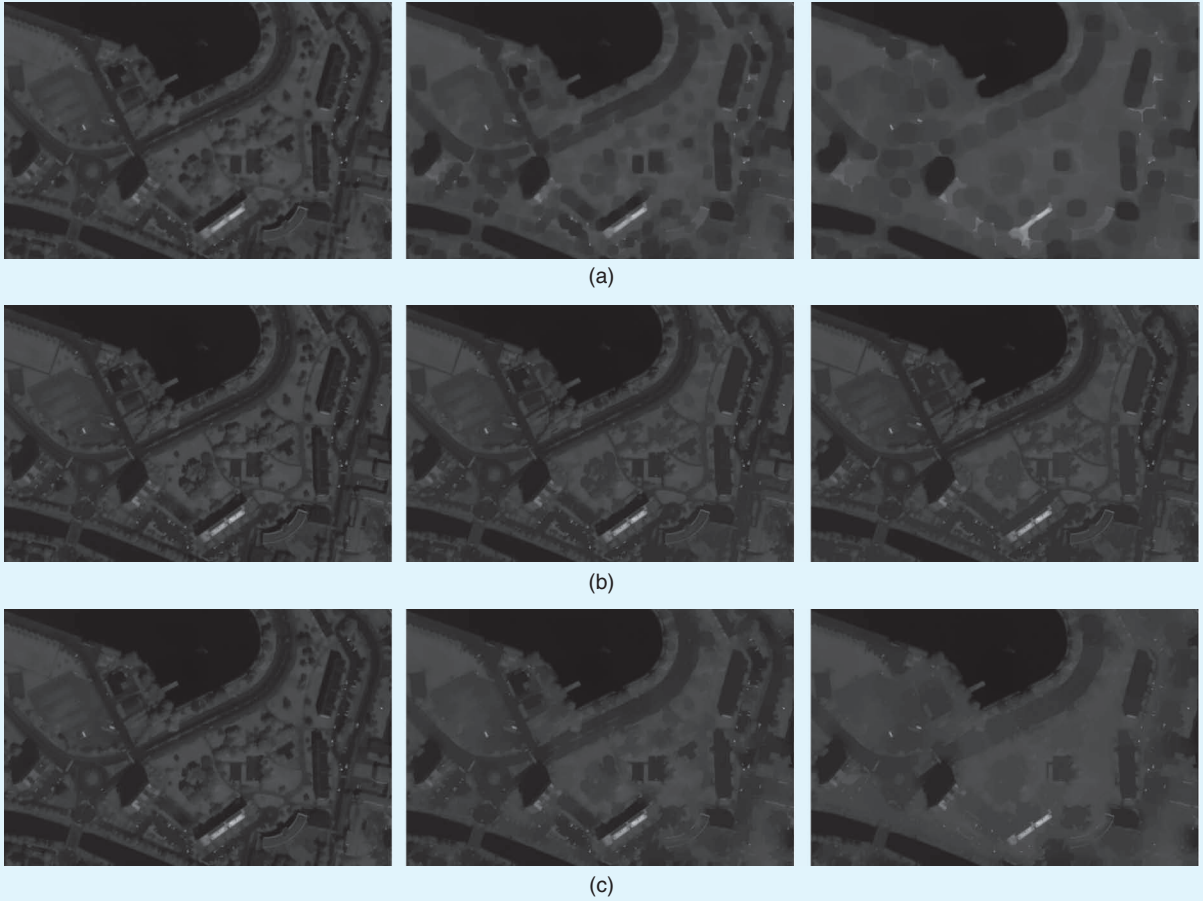
FIGURE 7. The closings with an increasing SE size on a Ghent Watersportbaan panchromatic image. The scales of the SEs vary from two to ten pixels with a step increment of four pixels. (a) Without reconstruction, (b) geodesic reconstruction, and (c) partial reconstruction.

where δ^1 represents elementary dilation [49] with the SE of elementary size and $\wedge$ represents the point-wise minimum. To perform the reconstruction by dilation $R_g(f)$ of f with g as the mask, we use the operator iteratively until no further change occurs:

$$R_g(f) = \lim_{n \to \infty} \delta_g^n(f) = \underbrace{\delta_g^1 \delta_g^1 \cdots \delta_g^1(f)}_{\text{until stability}}. \qquad (2)$$

An opening by reconstruction γ of an image f can be obtained by first performing a regular opening σ on the image f and then using the result of this opening as the marker image and the original image as the mask for the reconstruction process:

$$\gamma = R_f(\sigma(f)). \qquad (3)$$

Closing by reconstruction ϕ can be defined by duality (i.e., first invert the image, then perform the opening by reconstruction, and, finally, invert the result). With reconstruction, we can better preserve the shapes of the objects, as shown in Figures 5(b), 6(b), and 7(b). As the scale increases, more and more small objects disappear.

Morphological operators by reconstruction delete objects smaller than the SE without altering the shape of those objects and reconstruct connected components from the preserved objects. In other words, the pixels in the object take on the value of their surroundings. We use the term *scale* of an opening or closing to refer to this size. A vector containing the pixel values in openings and closings by the reconstruction of different scales is called the *MP*. The MP of size p (number of scales) can be defined as

$$MP^{(p)}(f) = [\phi^{(p)}(f), \ldots, \phi^{(1)}(f), f, \gamma^{(1)}(f), \ldots, \gamma^{(p)}(f)]. \quad (4)$$

The MP carries information about the size and shape of objects in the image.

ATTRIBUTE FILTERS

The AFs are morphological transformations that process an image per a criterion. A generic criterion P can be defined as a mapping of the set C of values $P : C \to \{\text{false, true}\}$. The AFs process connected components per the criteria that evaluates how an attribute A compares to a given reference value λ in a binary predicate P [e.g., $P(C) = A(C_i) > \lambda$, with C_i

being the ith connected component of the upper- or lower-level sets of an image]. If P holds true, then the region is kept unaltered; otherwise, the region can be set to the gray-scale value of the adjacent region with the closest gray level, thereby merging the connected components. When the region is merged to the adjacent region of a lower (or greater) gray level, the operation performed is a thinning (or thickening). A criterion is said to be increasing if it is verified for a connected component, in which case the criterion's components will also be increasing. This property leads to, e.g., $P(C_j) =$ true when $P(C_i) =$ true for any $C_j \subseteq C_i$.

When the criteria (e.g., the area and volume associated with increasing attributes) are increasing, the attribute thinning and thickening transformations are also increasing, leading to attribute opening and attribute closing [58], respectively. For nonincreasing criteria (e.g., gray-level homogeneity, shape descriptors, and region orientation), we recall that different outputs of the filter are obtained according to the filtering rules selected [48]. If P holds true for a connected component, it will be merged to a darker or brighter surrounding region according to the transformation. Given a sequence of ordered threshold values $\lambda = \{\lambda_1, \lambda_2, \ldots, \lambda_n\}$ (i.e., $\lambda_i <= \lambda_j$, with $i < j$), an AP is obtained by applying a sequence of attribute thinning and thickening operations to the gray-scale image f,

$$AP(f) = \{\varphi_n(f), \ldots, \varphi_1(f), f, \rho_1(f), \ldots, \rho_n(f)\}, \quad (5)$$

where φ_i and ρ_i denote the attribute thinning and thickening transformations with reference values λ_i, respectively. AFs process the image without distorting or inserting new edges but only by merging existing flat regions [7], as shown in Figures 8(a) and 9(a). Compared to MPs, the APs permit the modeling of other characteristics (e.g., geometrical, textural, and spectral) rather than the size of the objects. We refer the reader to [11] for further details.

However, as connected operators, both geodesic reconstruction [49] and AFs [11] suffer the same leakage effects (again, called *over-reconstruction* in [10]). Some objects that should disappear at a certain threshold, however, remain present after filtering, as shown in Figures 5(b), 6(b), 8(a), and 9(a). In LiDAR data [see Figure 6(b)], the residential roof and trees are connected and are similar in elevation characteristics; consequently, they are treated as a single object after reconstruction. As a result, different objects (even though they are in different categories) are considered as a single object if, in the original image, they are connected through a narrow line in the image. In typical remote-sensing scenes, many objects are arranged in a complex manner (such as the image in Figure 1), i.e., roads are connected to many other objects such as parking lots (with the same gray level) and buildings (with a different gray level). For example, objects P_{11}, P_{21} in Figure 3 are expected to disappear in the image when the sizes of the area attributes are set to 350 and 450, respectively [see Figure 8(a)]. However, they remain present even when the area size is set to 800 in the original attribute thinning and thickening [11]. While these two objects are assumed to remain the same with the MI [11] attributes of 0.3 and 0.8, they, however, disappear at MI values of 0.2 and 0.3, respectively [in Figure 9(a)]. This means that, in MPs/APs, the pixels from the road are not characterized by the attributes (e.g., size, area, and MI) of the road but by the attributes of the whole connected object (and these connected objects belong to different classes). Clearly, this leads to a poor performance on post applications.

MORPHOLOGICAL FEATURES WITH PARTIAL RECONSTRUCTION
To overcome the leakage effects, partial reconstruction is used for morphological operators and AFs. A MATLAB application that implements partial reconstruction for both morphological operators and AFs is available at http://telin.ugent.be/~wliao/Partial_Reconstruction/.

MORPHOLOGICAL OPERATORS BY PARTIAL RECONSTRUCTION
In the geodesic reconstruction process, a pixel is reconstructed if it is connected to another pixel that was not deleted after the opening or closing. In other words, a pixel is reconstructed if the geodesic distance d in the mask g of
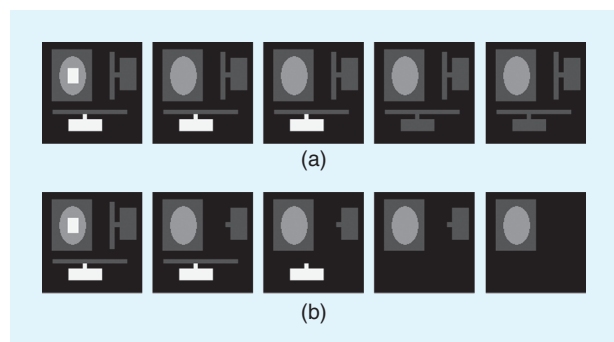

FIGURE 8. The attribute thinning with an area attribute on a synthetic image. From left: the size of the area was set to 200, 350, 450, 600, and 800 pixels. (a) Original attribute thinning and (b) attribute thinning with partial reconstruction.
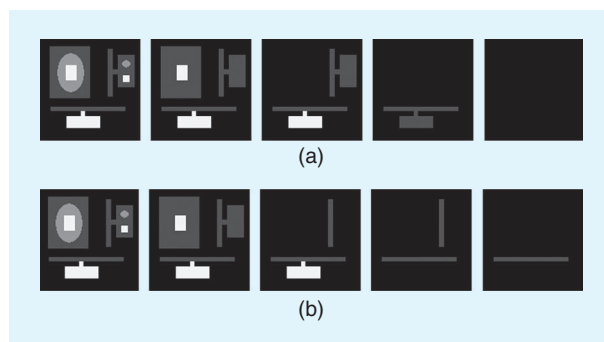

FIGURE 9. The attribute thinning with an MI attribute. From left: the value of the MI was set to 0.15, 0.17, 0.2, 0.3, and 0.8. (a) Original attribute thinning and (b) attribute thinning with partial reconstruction.

that pixel is less than infinite to at least one of the pixels in the marker image f [49], [50]. Generally, a geodesic distance is the minimum distance between two points on the Earth's surface. Note that this is not the length of a straight line (Euclidean distance) but the length of a segment of a circle. Similarly, the geodesic distance between two pixels is the length of the shortest path between those pixels. The path is not arbitrary, but it must be a subset of the foreground pixels of the image.

If we use the Euclidean distance (instead of the geodesic distance), a large object can influence a large part of a smaller object if both objects lie close to each other, even if the connection between them is very narrow. With the geodesic distance, only a small area of the smaller object near the connection is influenced. The study in [10] proposed a novel partial reconstruction in which a pixel is reconstructed if the geodesic distance is smaller than $d < \infty$. Opening with partial reconstruction [10], $\bar{\gamma}$ is defined as

$$\bar{\gamma} = \delta_f^d(\sigma(f)). \tag{6}$$

The partial reconstruction is the same as a geodesic dilation of size d [49], [50]. The easiest way to implement this is by doing successive elementary geodesic dilations, i.e., iterate (2) only d times. This is a dilation with an elementary SE followed by an intersection with the mask. In gray-scale morphology, the intersection of two images is the minimum of the two gray-scale values for each pixel. Instead of using the original image, we can obtain the mask for partial reconstruction by dilating the opening with a disk-shaped SE with radius d followed by the intersection with the original image.

For rectangular objects and with disk-shaped SEs, the geodesic distance can be set to $d = (\sqrt{2} - 1)R$ for partial reconstruction with R as the radius of the SE, but the corners of objects are not completely reconstructed when $d < (\sqrt{2} - 1)R$. In contrast, partial reconstruction with $d > (\sqrt{2} - 1)R$ completely reconstructs the corners of rectangular objects. Many objects of interest in remote sensed images have a near-rectangular shape. Therefore, we use a value of d near this value [e.g., $d = 2(\sqrt{2} - 1)R$] for partial reconstruction. For more details on morphological filters with partial reconstruction, we refer the reader to [10].

ATTRIBUTE FILTERS WITH PARTIAL RECONSTRUCTION
To overcome the leakage effects, AFs with partial reconstruction (AFsPR) [51] first separate connected objects (e.g., roads and parking lots) of a binary image (i.e., at one gray level) into two disjoint parts by using morphological filters with partial reconstruction [10]. We define two binary images to include each part of the separated object. Then AFs [11] are applied to these two binary images. Finally, AFsPR integrate all of the residuals of the filtered

images and obtain the final output image by repeating this for all gray levels. Suppose that f_i is the binary in gray level i and, for opening, f_i is referred to the upper-level set ($f_i = f > i$) while, for closing, f_i is the lower-level set ($f_i = f \leq i$). A connected object $\mathbf{P}_k$ (kth connected component) in f_i can be separated into two different adjacent and nonoverlapping parts $\mathbf{P}_{k1}$ and $\mathbf{P}_{k2}$ that satisfy $\mathbf{P}_k = \mathbf{P}_{k1} \cup \mathbf{P}_{k2}$ and $\mathbf{P}_{k1} \cap \mathbf{P}_{k2} = \varnothing$.

A binary image f_i can be partitioned in its connected components (here, we refer to foreground) $\mathbf{P}_1, \mathbf{P}_2, \ldots$, such that f_i is the union of all $\mathbf{P}_k$ and each $\mathbf{P}_k$ is a connected component with $\mathbf{P}_k \cap \mathbf{P}_l = \varnothing$ if $k \neq l$. Let $\bar{\gamma}^j$ and $\bar{\phi}^j$ denote morphological opening and closing operators by partial reconstruction using a structuring element of size j. For opening, morphological opening with partial reconstruction is first applied in the binary image f_i (at gray-level i). As the size of the SE j increases, more and more small, bright objects disappear. Two binary images, f_{i1}^o and f_{i2}^o, are defined as the filtering outs at scale j. $f_{i1}^o = \bar{\gamma}^j(f_i)$ contains one part of the connected objects $\mathbf{P}_{k1}$ in f_i, and $f_{i2}^o = f_i - f_{i1}^o$ includes all disappeared objects of f_i (i.e., the other parts of the connected objects $\mathbf{P}_{k2}$ of f_i).

In an opening, for gray-level i, we apply the binary attribute opening φ [58] on both binary images of f_{i1}^o and f_{i2}^o and integrate the remaining objects into one filtered image $\overline{f_i^o}$:

$$\overline{f_i^o} = \varphi(f_{i1}^o) + \varphi(f_{i2}^o). \tag{7}$$

When repeating (7) at each gray level, the attribute thinning with partial reconstruction is defined by the maximum gray level of the results of the filtering for each pixel x as

$$\bar{\varphi}_\lambda(f)(x) = \max\{i : x \in \overline{f_i^o}\}, \tag{8}$$

where $\lambda = \{\lambda_1, \lambda_2, \ldots, \lambda_n\}$ is a sequence of ordered criteria, which is the same as defined in [11]. The attribute thickening with partial reconstruction $\bar{\rho}$ can be straightforwardly extended from the definition of thinning. We refer the reader to [51] for further details.

Morphological/AP with partial reconstruction (APPR) can be obtained similarly as in (4) and (5) by replacing the connected filters by the filters with partial reconstruction. Thus, the partial reconstruction [10] solved the problem of over-reconstruction while preserving the shape of objects as much as possible and made a great improvement in the classification of remote sensing imagery [2], [20], [51], [53], [54]. As shown in Figures 5(c), 6(c), and 7(c), the shapes of objects are better preserved with partial reconstruction compared to the MP without reconstruction. However, some of the more complex shapes are not as well preserved as with connected filters. Yet many small objects that remain present in the profile generated by geodesic reconstruction and AFs now disappear when using the filters with partial reconstruction. We can see objects disappear per their real attribute values in

Figures 8(b) and 9(b). This is because in remote-sensing (urban) scenes, different objects lie closely together, and, because of noise and other effects, different objects are often connected by a sequence of pixels with similar (or more extreme) pixel values. Therefore, geodesic reconstruction and AFs consider all those connected objects as a single object, and objects only disappear when the SE does not fit the broadest part (for AFs, we take the area attribute as an example) of the connected object, even though this part might be far away from the actual object. Partial reconstruction reconstructs only the immediate surrounding area of the surviving part. The edges of simple objects are reconstructed well, but a full retrieval of complex elongated shapes might not be obtained. For simple objects such as rectangles, geodesic reconstruction and AFs are complete, because, in urban remote-sensing scenes, most objects are not very complex and the partial reconstruction of rectangular-shaped objects has been well suited.

EXTENSION TO THE ANALYSIS OF HYPERSPECTRAL IMAGERY

When dealing with hyperspectral imagery (or other vectorial images), the high dimensionality of hyperspectral data and the redundancy within the bands make the generation of MPs/APs based on each spectral band a time-consuming task. To overcome this problem, FE is first used as a preprocessing step to reduce the dimensionality of these hyperspectral data and reduce the redundancy within the bands. Then, morphological/attribute processing is applied on each extracted feature band independently. The effect of different FE methods on extracting features from the hyperspectral data to build MPs/APs has been discussed in several studies [54], [62], [63].

An MP/AP consists of the opening profile (OP) and the closing profile (CP). For the panchromatic image, the MP/AP is built on the original single-band image directly. The OP or CP with its p scale set at pixel $\mathbf{x}$ forms a p-dimensional vector. By incorporating the OP and the CP, an MP/AP of pixel $\mathbf{x}$ is defined as a $(2p+1)$-dimensional vector. Suppose that r features are extracted from the original hyperspectral data, EMPs/APs (named *EMP/EAP*) are defined by concatenating all MPs/APs computed on these r features [9]. The EMP of pixel $\mathbf{x}$ is an $r(2p+1)$-dimensional vector, and Figure 10 shows an EMP built on the first two PCs. Suppose that we want to construct n attributes [e.g., area and standard deviation (Std)] in λ_i ($i \in [1, n]$). For each attribute with the same scale (e.g., p thresholds), the EAP of pixel $\mathbf{x}$ is an $nr(2p+1)$-dimensional vector.

The selected features are rescaled to a defined range and converted to integer form to be processed by the AFs. When converting the intensities of the selected features from double to integer, it is not easy to determine a good range. For a high range, it increases the computational time. For a lower range, although reducing the processing time, the rescaled features are smoothed, which leads to unexpected effects (e.g., many objects are connected). These connected objects are often treated as a single object by original-attribute thinning and thickening, which consequently leads to reduced classification performances. Figures 11 and 12 show examples of features with different rescaled ranges using attribute thinning [11], [12]; for the attribute thinning with partial reconstruction [51], we normalize the resulting thinning for better visualization.
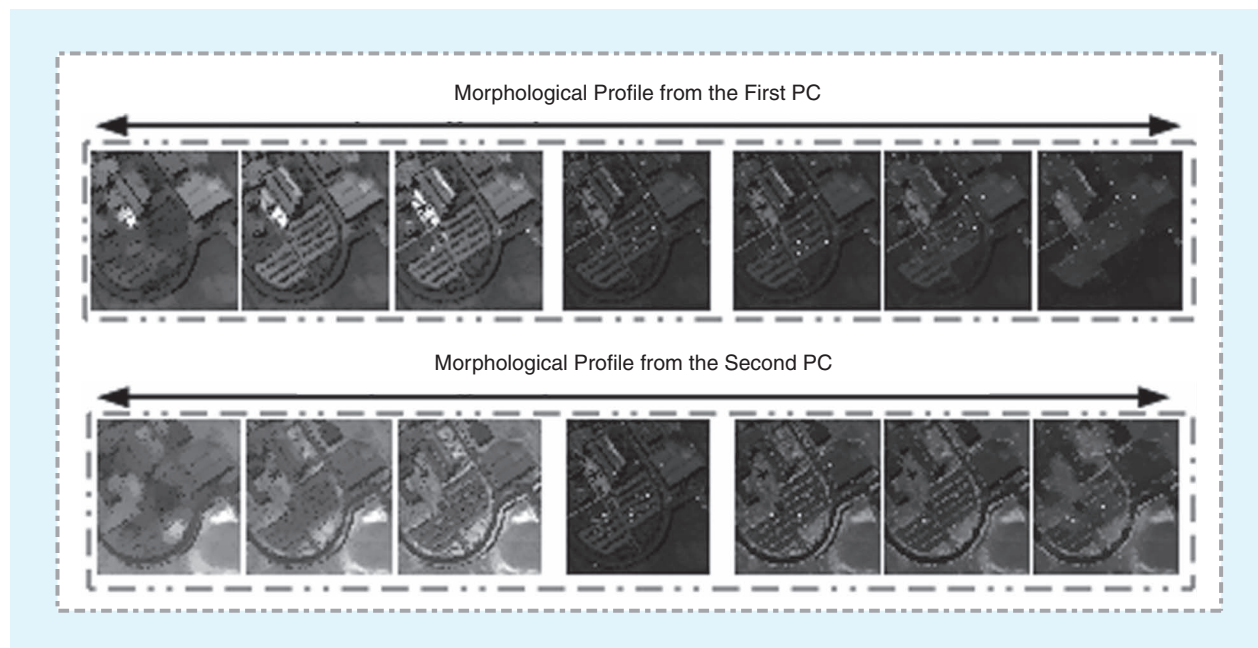

FIGURE 10. The EMP for a hyperspectral image. PC analysis is used as an example for FE, and the first two PCs are used to build the EMP.
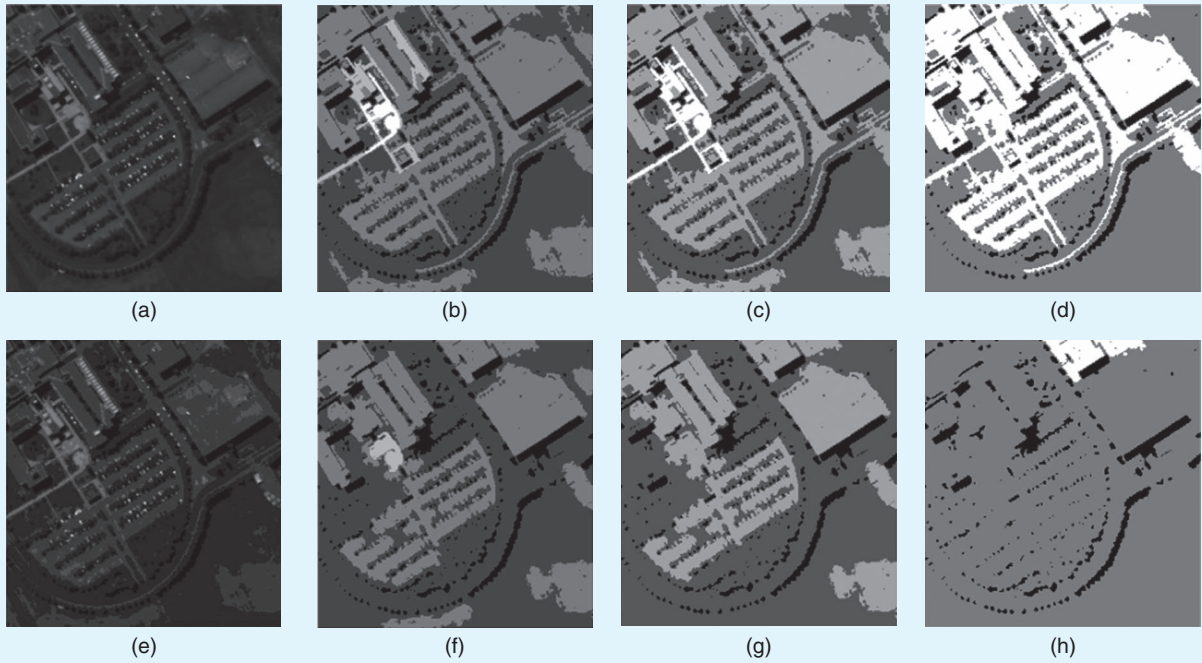
FIGURE 11. Examples of area AP computed with the first PC rescaled into the range [0, 10]. The scales of the area are in 500, 1,000, and 5,000 pixels. (a) The first PC of the University of Pavia, (b)–(d) the AP computed by original attribute thinning, (e) the PC rescaled into range [0, 10], and (f)–(h) the AP computed by using attribute thinning with partial reconstruction.
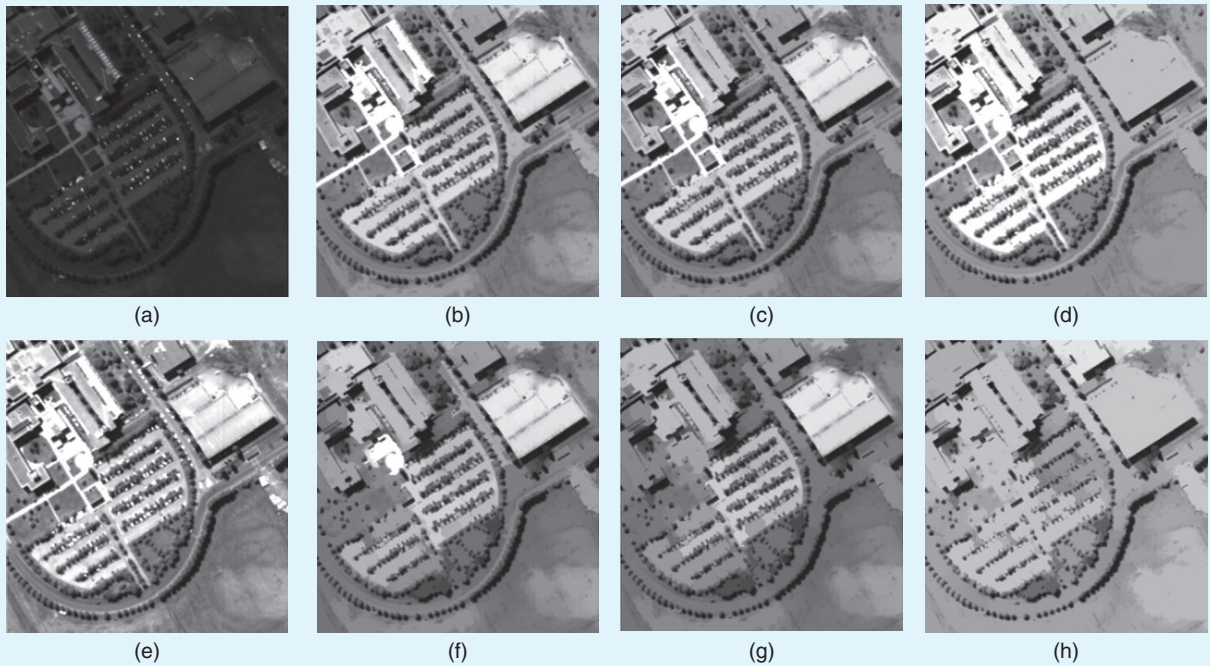

FIGURE 12. Examples of area AP computed with the first PC rescaled into the range [0, 1000]. The scales of the area are in 500, 1,000, and 5,000 pixels. (a) The first PC of the University of Pavia, (b)–(d) the AP computed by original attribute thinning, (e) the PC rescaled into range [0, 1,000], and (f)–(h) the AP computed by using attribute thinning with partial reconstruction.

The figures show that many small objects that should disappear at a certain scale of area attribute remain even at a very high scale when using attribute thinning [11], [12]. This is much worse when the selected features were rescaled to a lower range (e.g., [0, 10] in Figure 11). This is because more objects are connected as the ranges of the rescaled features set decrease. If the attributes of all connected objects are mixed together, these connected objects remain or disappear together. In these cases, the attribute thinning and thickening cannot well model the spatial information of the objects.

EXPERIMENTAL RESULTS

EXPERIMENTAL SETUP

To generate MPs, we apply a circular SE with ten openings and ten closings (ranging from one to ten with a step-size increment of one). For the construction of the APs, we consider three different attributes: 1) a, area of the regions; 2) s, Std of the gray-level values of the pixels in the regions; and 3) i, first moment invariant of Hu, MI. The area extracts information on the scale of the objects. The Std and MI are not dependent on the size dimension, but they are related to the geometry of the objects and the homogeneity of the intensity values of the pixels, respectively. All of the images were rescaled to the range [0, 255] and converted to integer form to be processed by the AFs. The values of different attributes are $\lambda_a = [100, 500, 1,000, 2,000, 3,000, 4,000, 5,000, 6,000, 7,000, 8,000], \lambda_s = [0.1, 0.5, 1, 2, 3, 4, 5, 6, 7, 8]$, and $\lambda_i = [0.1, 0.15, 0.2, 0.25, 0.3, 0.35, 0.4, 0.45, 0.5, 0.55]$.

Prior to applying morphological openings and closings (or the attribute thinning and thickening) to the hyperspectral image, PCA was first applied to the original hyperspectral data set, and the first few PCs (the first three PCs for the University of Pavia) were selected (representing 99% of the cumulative variance) to construct the EMPs. To compare MPs and APs by reconstruction with those by partial reconstruction, we consider both information redundancy and their post applications to classification. We use a support vector machine (SVM) [59] classifier, as it performs well on the classification of high-dimensional and/or multiple features [26], even with a limited number of training samples, limiting the Hughes phenomenon [60]. The SVM classifier with radial-basis function (RBF) kernels in the MATLAB SVM Toolbox, a library for SVMs [61], is applied in our experiments. An SVM with RBF kernels has two parameters, i.e., the penalty factor C and the RBF kernel widths γ. We apply a grid search on C and γ using five-fold cross-validation to find the best C within the given set $\{10^{-1}, 10^0, 10^1, 10^2, 10^3\}$ and the best γ within the given set $\{10^{-3}, 10^{-2}, 10^{-1}, 10^0, 10^1\}$.

We compared the following schemes: original image (Raw); morphological profiles with no reconstruction (MPNs), morphological profiles with geodesic reconstruction (MPRs), morphological profiles with partial reconstruction (MPPRs); each single existing AP (AP_a, AP_s, and AP_i); and single APPR ($APPR_a$, $APPR_s$, and $APPR_i$). We also com-

pared the performances of stacking all APs or APPRs together, which are defined as EAP and extended APPR (EAPPR) [EMP and EMP with reconstruction (EMPPR) for EMPs, respectively].

The performances of each scheme are quantitatively evaluated by measuring the following metrics:

1) the normalized mutual information (NMI) that tests the independence between two variables and measures the information that they share

$$\text{NMI}(f,g) = \frac{\text{MI}(f,g)}{\sqrt{\text{MI}(f,f)}\sqrt{\text{MI}(g,g)}}, \qquad (9)$$

where the mutual information

$$\text{MI}(f,g) = \sum_{x \in f} \sum_{y \in g} p(x,y) \log\left(\frac{p(x,y)}{p(x)p(y)}\right), p(x,y)$$

is the joint probability distribution function of f and g, and $p(x)$ and $p(y)$ are the marginal probability distribution functions of f and g, respectively.

2) the overall accuracy (OA) calculating the number of correctly classified samples divided by the number of all test samples
3) the average accuracy (AA) denoting the average of class classification accuracy
4) the kappa coefficient of agreement (K) measuring the percentage of agreement corrected by the amount of agreement that could be expected due to chance alone [64]
5) the specific class accuracy representing the percentage of accurately classified samples for a given class.

Note that for 1), an NMI close to zero indicates independence, while a high NMI indicates dependence and feature redundancy [63].

INFORMATION REDUNDANCY: RECONSTRUCTION VERSUS PARTIAL RECONSTRUCTION

The most popular MPs/APs generated by using morphological reconstruction (including geodesic reconstruction and AFs) [11], [12] contain redundant information, because the connected objects survive in many scales. To test this assumption, we take a Ghent Watersportbaan panchromatic image as an example to compare the NMI among each profile (see Figures 13 and 14). These figures show that the MPNs contain the least redundancy with the lowest NMI among profiles. Figures 5(a), 6(a), and 7(a) show that objects smaller than the SE will disappear.

Morphological reconstruction [11], [12] cannot model the spatial information of the connected objects well in VHR images. Objects that are expected to disappear in the image at a low scale are still present at the highest scales, as is shown in Figures 5–9, 11, and 12. This is why additional geometrical features generated with morphological reconstruction [11], [12] have the highest NMI, i.e., contain much more redundant information. To reduce the redundancy, some algorithms were developed to automatically select a threshold for morphological APs [65]. Recently, some artificial intelligence
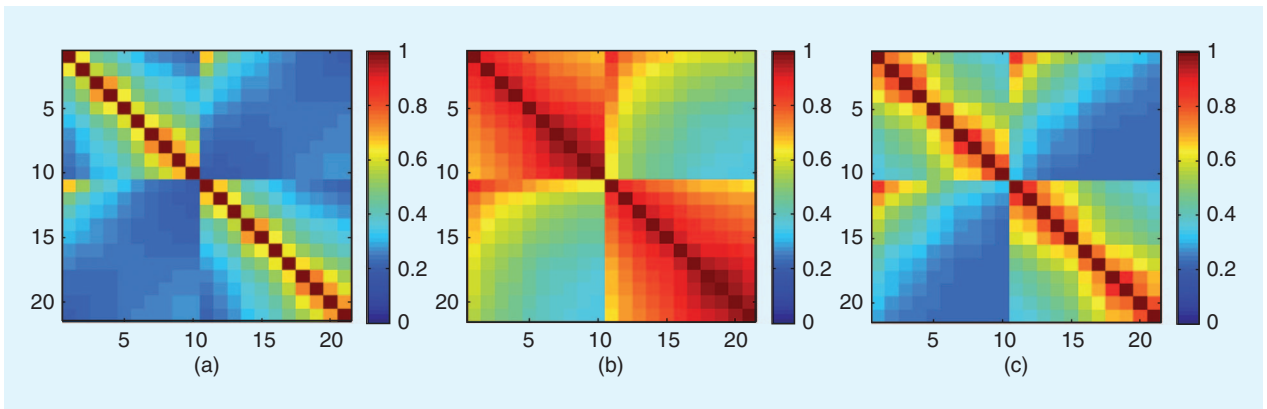
FIGURE 13. The mutual information matrices for MPs of a Ghent Watersportbaan panchromatic image: (a) MPNs, (b) MPRs, and (c) MPPRs.
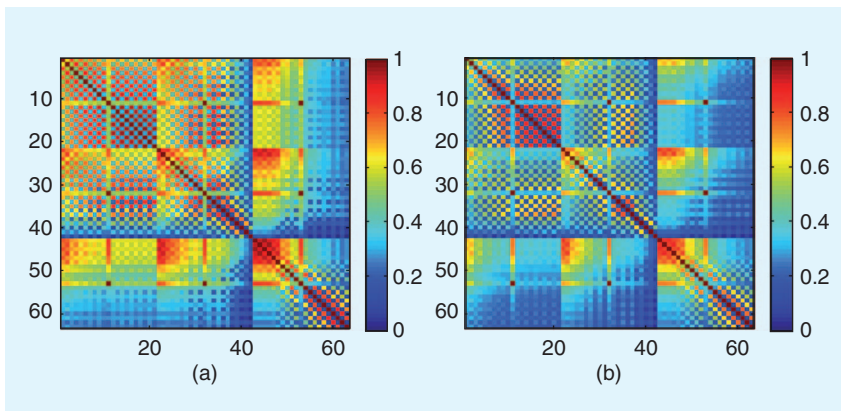

FIGURE 14. The mutual information matrices for all APs (including area, Std, and MI) of a Ghent Watersportbaan panchromatic image: (a) original APs and (b) APPRs.

algorithms were used for optimal feature selection in APs [39]. However, this increases the processing time. Moreover, the leakage problems cannot be solved.

With partial reconstruction, we not only better preserve the shapes of the objects (compared to those without reconstruction) but also greatly reduce the information redundancy contained in the generated profiles (compared to those with reconstruction). The connected objects are separated and merged to a darker (opening) or brighter (closing) surrounding region per their real attributes. Consequently, the partial reconstruction treats the connected objects well and better models the spatial information of the VHR remote-sensing imagery [10], [51]. The next question is: Can this information benefit post applications?

APPLICATIONS ON CLASSIFICATION: RECONSTRUCTION VERSUS PARTIAL RECONSTRUCTION

RESULTS ON THE GHENT WATERSPORTBAAN PANCHROMATIC IMAGE

We investigate the capability of the panchromatic image to produce land-use maps of the urban scene described in the

"Data Sets" section. The results are reported in Table 3, and the classification maps are shown in Figure 15. The simple and direct way to produce a land-use map exploits only panchromatic information with SVM classifiers. As expected, the results obtained appeared to be poor in terms of classification accuracy. The obtained K value is 0.40. Several of the defined classes were not recognized, such as classes of dark roof and red roof. Even though water, shadow, and asphalt are different, it is well known from the literature that they may assume similar intensities in panchromatic data. This has led to some confusion, where water is misclassified as shadows while dark roofs have been grouped to road, as shown in Figure 15(a).

To overcome the spectral deficit of panchromatic imagery, mathematical morphology is one of the most popular ways to extract additional information to improve the recognition of the objects within the scene. Compared to the situation with only panchromatic imagery, there is a 10–25% improvement with additional features modeled by mathematical morphology. Regarding the global accuracies, using the features with partial reconstruction yields a significant improvement when compared to that both with and without reconstruction. APPRs produced the best results on OA, AA, and K; and they lead to a significant increase of the classification accuracies, with 24% OA improvement over using only raw data, 5–9% OA improvements over using MP, and 7–17% OA improvements over the conventional APs.

For MPs, it is better not to use geodesic reconstruction. The OA of geodesic reconstruction is much lower than those without reconstruction and with partial reconstruction. For different man-made classes (e.g., dark roof, red roof, and road), which are typically connected in a remote-sensing scene, the

TABLE 3. THE GHENT WATERSPORTBAAN PANCHROMATIC IMAGE: CLASSIFICATION ACCURACIES OBTAINED BY ORIGINAL APs AND APPRs (THE VALUES WITH THE HIGHEST ACCURACY ARE IN BOLD).

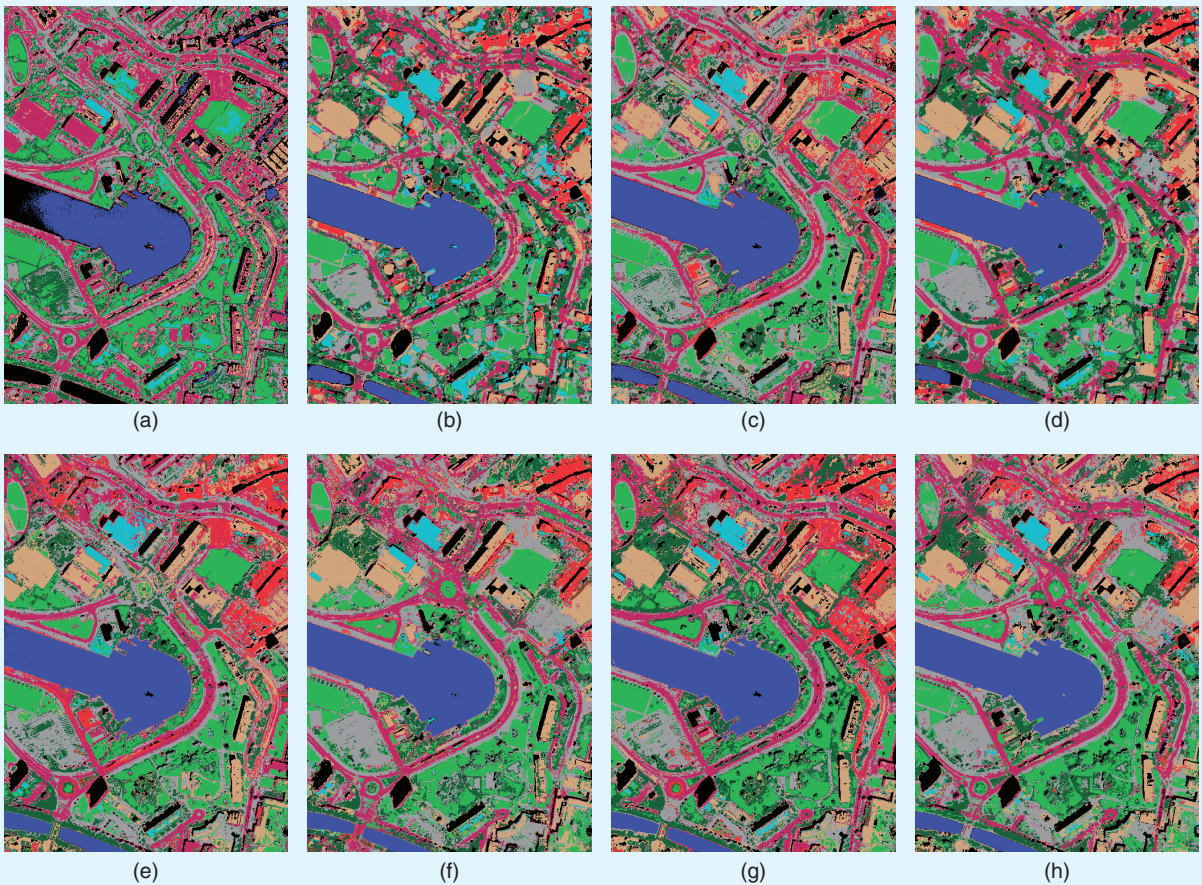|	RAW	MPNs	MPRs	MPPRs	ORIGINAL APs			AP_s	APPRs			$APPR_s$
					AP_a	AP_s	AP_i		$APPR_a$	$APPR_s$	$APPR_i$	
Number of features	1	21	21	21	21	21	21	63	21	21	21	63
OA (%)	48.29	66.57	63.87	67.0	64.22	60.24	55.77	65.52	70.80	67.29	57.49	**72.10**
AA (%)	46.84	72.80	68.65	71.40	68.87	65.38	60.75	70.89	75.84	71.67	57.80	**76.63**
K	0.40	0.612	0.580	0.616	0.585	0.541	0.491	0.601	0.659	0.619	0.505	**0.674**
Water	71.44	98.34	99.14	98.16	99.62	99.68	93.09	99.63	99.79	99.63	91.85	**99.84**
Grass	72.21	69.75	72.80	72.23	74.66	72.86	67.94	74.68	76.52	**77.19**	68.75	74.60
Trees	35.01	51.72	40.90	**53.81**	42.19	36.74	41.75	53.72	44.39	42.22	34.710	50.47
Dark roof	18.53	60.52	52.48	55.83	54.51	42.30	32.14	54.39	62.11	53.46	40.22	**63.85**
Red roof	0.0	**83.75**	66.64	72.41	65.05	53.78	47.55	71.75	83.55	66.18	20.89	78.98
White roof	61.05	91.25	86.61	84.07	87.87	91.18	85.29	89.92	89.68	**91.67**	73.12	90.76
Road	57.76	63.59	59.60	67.41	57.71	59.85	56.89	57.91	68.04	64.02	64.78	**72.72**
Other man-made	34.24	51.52	54.05	51.35	52.26	45.53	36.77	46.67	**70.29**	62.91	44.57	67.98
Shadows	71.32	84.75	85.61	87.35	85.95	86.48	85.30	89.32	88.21	87.79	81.35	**90.44**

FIGURE 15. The classification maps for the Ghent Watersportbaan panchromatic image. Thematic maps using (a) a raw panchromatic image, (b) MPNs, (c) MPRs, (d) MPPRs, (e) AP_a, (f) $APPR_a$, (g) APs (stacking all individual attributes together), and (h) APPRs.

confusion among them increases. However, without reconstruction, the boundaries of some objects are deformed in the classification map, as shown in Figure 15(b). The partial reconstruction is a tradeoff between reconstruction and

no reconstruction. This also shows in the global accuracies, which are comparable with the case of no reconstruction. The classification maps in Figure 15(b), (c), and (d) show that partial reconstruction produces smoother land-use maps than

TABLE 4. THE UNIVERSITY OF PAVIA HYPERSPECTRAL IMAGE: CLASSIFICATION ACCURACIES OBTAINED BY ORIGINAL APs AND APPRs (THE VALUES WITH THE HIGHEST ACCURACY ARE IN BOLD).

	RAW	EMPNs	EMPRs	EMPPRs	ORIGINAL APs				APPRs			
					AP_a	AP_s	AP_i	EAP	$APPR_a$	$APPR_s$	$APPR_i$	EAPPR
Number of features	103	63	63	63	63	63	63	189	63	63	63	189
OA	79.75	88.16	85.48	90.10	85.90	91.97	79.68	88.17	89.73	93.80	85.87	**97.52**
AA	88.26	84.75	90.10	88.16	91.93	91.90	85.26	92.37	93.95	94.29	90.65	**97.47**
K	0.747	0.841	0.811	0.866	0.819	0.895	0.740	0.847	0.866	0.918	0.819	**0.967**
Asphalt	84.17	82.43	94.54	87.06	94.90	92.95	90.11	95.39	91.72	93.98	91.40	**95.46**
Meadows	67.42	97.98	81.45	98.84	77.53	92.91	74.05	82.44	86.99	94.39	79.45	**99.51**
Gravel	73.70	50.64	72.84	69.03	77.89	69.99	58.46	73.51	**95.57**	93.66	72.80	94.90
Trees	94.78	90.54	97.06	91.09	95.14	89.20	90.34	97.23	96.31	83.29	93.96	**98.34**
Metal sheets	99.63	99.93	99.93	**100.0**	99.93	**100.0**	99.85	**100.0**	**100.0**	99.93	99.93	**100.0**
Soil	92.30	62.42	66.30	59.38	82.80	**98.97**	73.08	84.11	77.51	95.61	86.46	91.57
Bitumen	91.20	80.38	99.62	89.85	**99.85**	99.25	99.55	99.77	99.62	95.34	96.02	99.70
Bricks	91.47	98.89	99.24	98.40	99.48	84.71	81.99	99.05	98.02	92.42	**95.95**	97.75
Shadows	99.68	99.58	99.89	99.79	99.89	**100.0**	99.89	99.79	99.79	**100.0**	99.89	**100.0**

EMPRs: EMPs with geodesic reconstruction.

reconstruction and much better preserved shapes and borders than with no reconstruction.

For APs, AFsPR outperform conventional AFs on both individual attributes and stacking all attributes together. The improvements of partial reconstruction in terms of OA are 6, 7, and 2% for attributes of area, Std, and MI, respectively, compared with those of convention APs. The attribute of area produces better global accuracies than other attributes. With partial reconstruction, the confusion between the road and roofs decreases, and the accuracies of the dark roof and road classes increase by almost 10%. This is because dark roofs and roads are typically connected, which means they are treated as the same object by conventional AFs, leading to poor performances for post classification. Partial reconstruction can separate the connected objects, better model their attributes, and enable improved classification results.

> **MANY OBJECTS ARE MADE OF THE SAME MATERIAL (E.G., ROOFS AND ROADS ARE MADE WITH THE SAME ASPHALT); CONSEQUENTLY, USING ONLY SINGLE SPECTRAL FEATURES IS NOT ENOUGH FOR A RELIABLE CLASSIFICATION.**

RESULTS ON THE UNIVERSITY OF PAVIA HYPERSPECTRAL IMAGE

A hyperspectral image contains much richer information than a panchromatic image. The hyperspectral remote-sensing data from an urban area is a mix between man-made structures and natural materials. Many objects are made of the same material (e.g., roofs and roads are made with the same asphalt); consequently, using only single spectr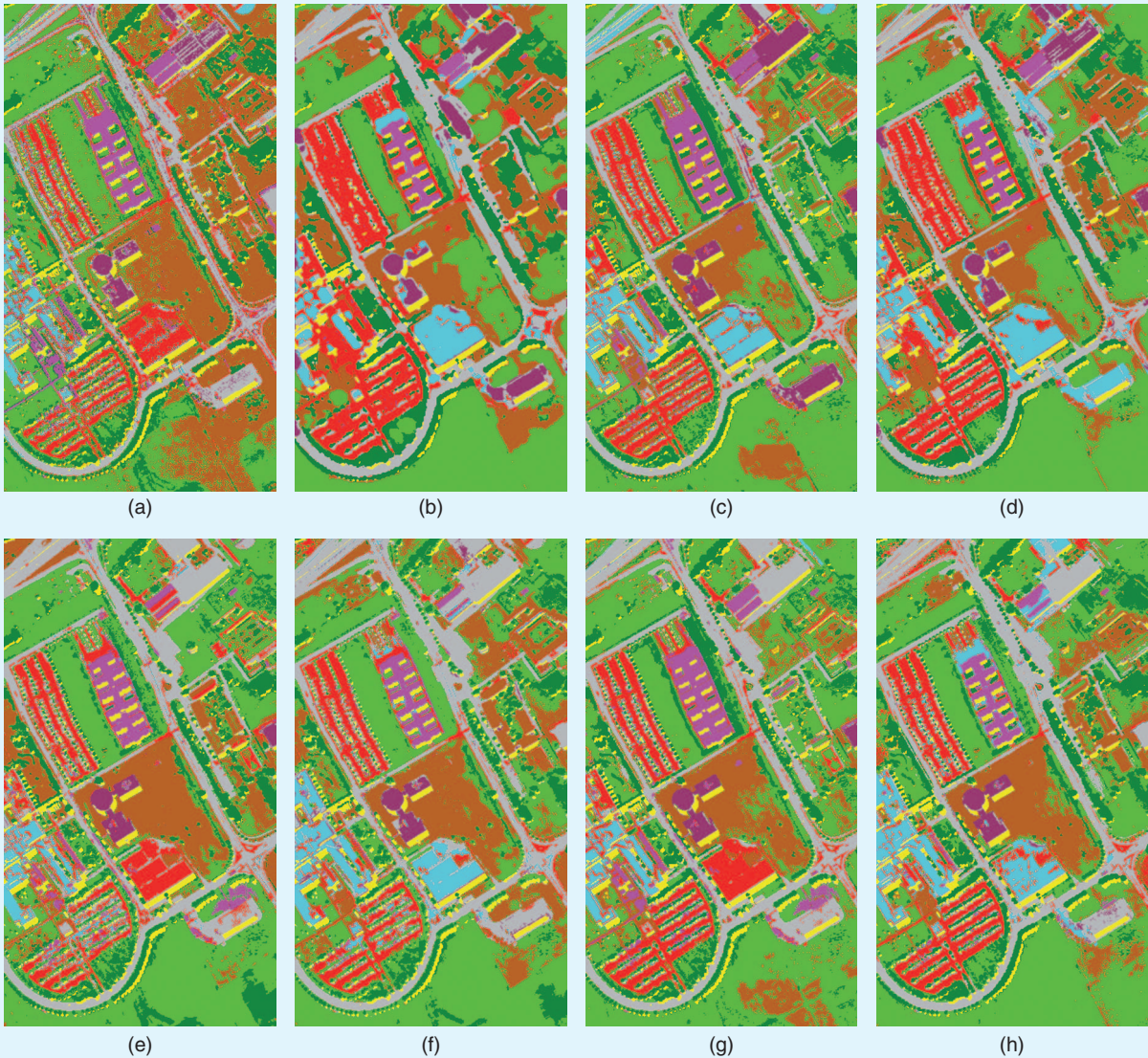al features is not enough for a reliable classification. We survey the extension of MPs and APs to the analysis of a hyperspectral image. Table 4 reports the accuracies, and Figure 16 shows the land-use maps.

The results confirm that including the additional spatial information modeled by mathematical morphology in the analysis resulted in higher accuracies (up to 20% of *K*) than those obtained by considering only the spectral information. The EAPPR produces the best results, with 17% OA improvements over using only raw hyperspectral data, 7–12% OA improvements over EMP [including EMP without reconstruction (EMPN), EMP, EMPPR], 4–17% OA improvements over using a single attribute (e.g., area, Std, or MI), and 9% OA improvements over the EAP generated by using original AFs [12].

When using the original AFs, it is sometimes better to use single APs than simply stacking many of them for classification. The original EAP produces worse results than only using single APs built with Std attribute, with OA dropping more than 3%. For each single AP, the APPRs constructed using the AFsPR [51] perform better than APs constructed by the existing AFs [12]. The improvements of APPRs over APs are almost 4, 2, and 6% for area, Std, and MI attributes, respectively. Moreover, stacking all single APPRs that are generated by partial reconstruction enables much better performances on classification. The EAP generated using original AFs contains redundant information because some connected objects survive in many scales (see Figure 12). That is why EAP sometimes performs even worse than single APs, which will be much worse when the selected PCs are rescaled into a lower range (see Figure 11 and discussions in [51]).

EMPs present similar conclusions as the Ghent Watersportbaan panchromatic image. APs outperform MPs

FIGURE 16. The classification maps for the University of Pavia. Thematic maps using (a) a raw hyperspectral image, (b) EMPNs, (c) EMPRs, (d) EMPPRs, (e) AP$_S$, (f) APPR$_S$, (g) EAPs, and (h) EAPPRs.

because the attribute of the Std produces better global accuracies than other attributes. With original APs, there is a large amount of confusion between gravel and bricks and meadows and soil. We see a clear improvement when using APPRs, and most of the gravel and meadows are now well classified.

RESULTS ON THE UNIVERSITY OF HOUSTON LiDAR DATA
Recent advances in airborne LiDAR technology allow us to rapidly measure topographical information over large areas. LiDAR remote sensing data have been widely used in many applications, e.g., forest management, urban planning, and disaster predictions. However, extracting useful information from LiDAR data remains challenging, especially in urban remote sensing where many objects have

the same elevation and are connected, such as roads and parking lots, trees, and buildings. We analyze the use of mathematical morphology to extract additional information for land-use classification. The resulting accuracies are reported in Table 5, and the classification maps are shown in Figure 17.

With only elevation information from raw LiDAR data, there is a large amount of confusion between water and soil and between the different man-made classes. When adding additional information extracted by mathematical morphology, we see a clear improvement with K over 20–45%. Consequently, the soil and road classes are better distinguished. This data set is very challenging for classification because the elevation information is very similar in some classes (e.g., tree and residential, grass stressed and

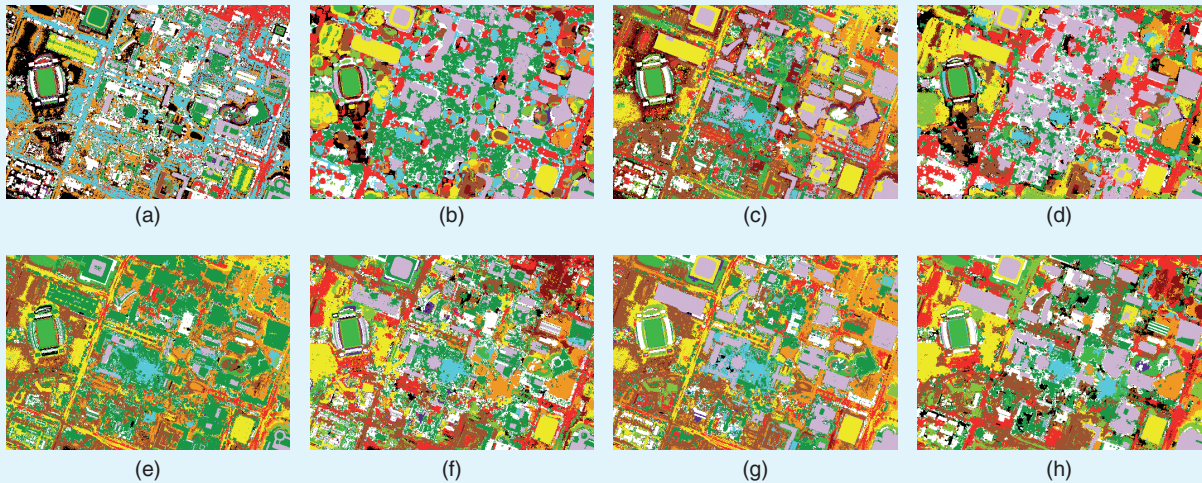|	RAW	MPNs	MPRs	MPPRs	ORIGINAL APs				APPRs			
					AP_a	AP_s	AP_i	APs	$APPR_a$	$APPR_s$	$APPR_i$	APPRs
Number of features	1	21	21	21	21	21	21	63	21	21	21	63
OA	31.34	65.86	57.69	68.31	55.08	51.73	53.73	63.65	69.97	59.26	57.85	**72.66**
AA	37.57	68.76	63.92	70.18	58.37	55.65	56.89	65.33	72.67	63.28	62.05	**74.81**
K	26.53	63.11	54.24	65.63	51.47	47.96	49.88	60.57	67.41	55.94	54.32	**70.31**
Grass healthy	35.90	37.51	44.16	48.05	60.02	61.63	63.44	61.63	60.97	70.47	62.58	**76.16**
Grass stressed	2.73	50.19	45.02	**66.54**	42.39	16.64	24.91	49.81	51.88	18.80	39.00	62.12
Grass synthetis	87.92	**97.82**	94.26	94.85	86.34	86.34	87.52	86.34	88.12	85.35	91.09	88.71
Tree	40.34	78.88	65.34	70.74	55.40	68.28	**90.72**	71.40	68.56	75.47	60.32	73.20
Soil	14.49	73.30	70.46	79.36	28.41	35.61	33.05	36.08	79.83	78.50	80.30	**89.77**
Water	70.63	63.64	86.71	78.32	68.53	64.34	78.32	70.63	78.32	76.92	81.82	**88.11**
Residential	57.37	68.38	65.21	70.80	66.14	60.63	35.07	74.35	**77.71**	54.85	58.40	69.50
Commercial	14.62	**96.39**	73.31	90.31	70.09	52.90	37.42	65.81	62.77	54.23	42.55	71.51
Road	22.0	50.71	40.89	**60.06**	49.95	37.58	47.21	53.45	57.44	53.26	34.37	47.78
Highway	5.50	38.32	34.75	44.21	27.61	37.45	54.05	64.09	58.98	36.78	47.20	**65.83**
Railway	67.65	81.31	43.55	79.41	89.37	96.77	90.82	**98.86**	89.75	76.85	88.24	98.48
Parking lot 1	12.10	55.24	49.38	54.47	44.67	27.76	47.17	56.96	**74.35**	51.30	38.81	57.44
Parking lot 2	11.93	58.60	63.51	**69.12**	61.75	62.46	39.65	65.61	62.81	67.37	61.05	63.51
Tennis court	93.12	**100.0**	98.38	68.83	97.17	97.17	96.36	97.17	99.60	**100.0**	89.07	89.88
Running track	27.27	81.18	**83.72**	77.59	27.70	29.18	27.70	27.70	81.61	49.05	56.03	80.13

FIGURE 17. The classification maps for the University of Houston LiDAR data. Thematic maps using (a) a raw hyperspectral image, (b) MPNs, (c) MPRs, (d) MPPRs, (e) AP_m, (f) $APPR_m$, (g) APs, and (h) APPRs.

soil, and road and parking lot 1). Moreover, these objects are connected in typical remote-sensing scenes. That is why geodesic reconstruction (even original APs) performs much worse than those with no reconstruction and with partial reconstruction, with OA decreases that are almost 2–10%. Many classes are misclassified, grass stressed and soil are confused, and road and parking lot 1 are confused. Working as connected filters, geodesic reconstruction and conventional AFs treat connected objects (even in different classes) as a single object. Without reconstruction, the borders of rectangular objects are obviously degraded to round ones. With partial reconstruction, the classification performances are greatly improved. APPRs produce the best OA, AA, and *K*, with 7% OA improvements over MPNs and 9% OA improvements over APs. With partial reconstruction, the OA improvements over original APs are 14, 8, and 4% for the attribute of area, Std, and MI, respectively.

CONCLUSIONS

In this article, morphological partial reconstruction is introduced for the analysis of VHR images. Morphological reconstruction (including geodesic reconstruction and AFs) has been widely used to extract additional spatial information from raw images to improve the performances of many applications (e.g., classification and change detection). However, conventional morphological reconstruction suffers from leakage problems. Objects expected to disappear at a certain threshold remain present when they are connected with other objects in the image. The attributes of small objects are mixed with their larger connected objects, which leads to poor performances on post applications. The main objective of this article is to address a common situation in existing morphological reconstruction where the attributes of the connected objects in an image are not well modeled. A main contribution of partial reconstruction is that it can separate connected objects and thus better model the spatial information of objects in an image and enable improved performances for post applications.

The experiments on a variety of urban remote-sensing scenes, including panchromatic, hyperspectral, and LiDAR images, confirmed the expected improvements of partial reconstruction over conventional reconstruction. The improvements become more significant when more objects from different classes are connected or all single attributes are stacked together. The literature shows that APs can outperform MPs as they can model higher-level features (not only size and shape but also homogeneity and contrast). However, in some typical remote-sensing scenes, where many man-made objects are arranged in a complex manner (e.g., roads are connected to parking lots and buildings in panchromatic or hyperspectral scenes, or trees and roofs have similar elevation and are connected in LiDAR scenes), it is better to use MPPRs than conventional AFs. Moreover, when extending the conventional APs to hyperspectral images, it is sometimes better to use a single AP instead of simply stacking them together (i.e., the EAP) for post applications. The profiles generated by conventional reconstruction contain redundant information because objects survive in many scales if connected with larger objects. Future work will include but is not limited to the following topics:

1) Speeding up the AFsPR by borrowing some ideas from second-generation connectivity [45], [46]. A simple possible solution is to first partition an image into two non-overlapping parts to separate the connected objects. Then, the original AFs can be done in parallel on both parts. The filtering results of both parts can be merged to obtain the final output. Another efficient solution is to construct a max-tree and min-tree data structure based on the appropriate connectivity so that leakage can be prevented and attributes can be computed on this tree. Fast implementation of the current version of partial reconstruction can exploit the use of commodity graphics processing units (GPUs) or multi-GPU platforms.

2) The fusion of multiple-level features for remote-sensing image interpretation. The state-of-the-art fusion methods typically manage either lower-level or high-level features but not a combination of both. For example, morphological operators were employed in [9], [10], [20], and [26] to extract low-level features (such as the size and shape of objects) from remote-sensing images. In [38], middle-level attribute features were extracted from both optical and LiDAR images for land-cover mapping. High-level features, such as semantic information indexes [13]–[15] and so-called deep learning features, have been used for change detection and classification. The features extracted at each level have their own characteristics, i.e., high-level features are usually more powerful but less robust, while low-level ones are less informative but more reliable. Combining complementary features from multiple levels for better interpretation remains challenging.

AUTHOR INFORMATION

Wenzhi Liao (wenzhi.liao@ugent.be) received his B.S. degree in mathematics from Hainan Normal University, HaiKou, China, in 2006, his Ph.D. degree in engineering from South China University of Technology in 2012, and his second Ph.D. degree in computer science engineering from Ghent University, Belgium, in 2012. Since 2012, he has been working as a postdoctoral scholar at Ghent University and is a postdoctoral fellow with the Fund for Scientific Research in Flanders. His current research interests include pattern recognition, remote sensing, and image processing. In particular, he is interested in mathematical morphology, multitask feature learning, multisensor data fusion, and hyperspectral image restoration. He is a member of the IEEE Geoscience and Remote Sensing Society (GRSS) and the IEEE GRSS Data Fusion Technical Committee. He is a Senior Member of the IEEE.

Jocelyn Chanussot (jocelyn.chanussot@gipsa-lab .grenoble-inp.fr) received his M.Sc. degree in electrical engineering from Grenoble Institute of Technology, France, in 1995 and his Ph.D. degree from the Universitè de Savoie, Annecy, France, in 1998. He is a professor of signal and image processing at Grenoble Institute of Technology. He is currently conducting research at the Grenoble Images Speech Signals and Automatics Laboratory. He is also an

adjunct professor of the University of Iceland, Reykjavík. His research interests include image analysis, multicomponent image processing, nonlinear filtering, and data fusion in remote sensing. He is the founding president of the IEEE Geoscience and Remote Sensing French Chapter (2007–2010) and an associate editor for *IEEE Transactions on Geoscience and Remote Sensing*. He is a Fellow of the IEEE and a member of the Institut Universitaire de France.

Mauro Dalla Mura (mauro.dalla-mura@gipsa-lab .grenoble-inp.fr) received his laurea (B.E.) and laurea specialistica (M.E.) degrees in telecommunication engineering from the University of Trento, Italy, in 2005 and 2007, respectively. He received a joint Ph.D. degree in information and communication technologies (telecommunications area) from the University of Trento and in electrical and computer engineering from the University of Iceland, Reykjavík, in 2011. He is an assistant professor at Grenoble Institute of Technology, France. He is conducting research at the Grenoble Images Speech Signals and Automatics Laboratory. His main research interests include remote sensing, image processing, and pattern recognition. In particular, he is interested in mathematical morphology, classification, and multivariate data analysis. He has been the president of the IEEE Geoscience and Remote Sensing Society French Chapter since 2016 and is on the editorial board of *IEEE Journal of Selected Topics in Applied Earth Observations and Remote Sensing*. He is a Member of the IEEE.

Xin Huang (huang_whu@163.com) received his Ph.D. degree in photogrammetry and remote sensing from Wuhan University, China, in 2009, working with the State Key Laboratory of Information Engineering in Surveying, Mapping, and Remote Sensing. He is a full professor with Wuhan University, where he teaches remote sensing, photogrammetry, and image interpretation. He is the founder and director of the Institute of Remote Sensing Information Processing, School of Remote Sensing and Information Engineering, Wuhan University. His research interests include hyperspectral data analysis, high-resolution image processing, pattern recognition, and remote sensing applications. He also serves as an associate editor of *Photogrammetric Engineering and Remote Sensing* and *IEEE Geoscience and Remote Sensing Letters*. He is a Senior Member of the IEEE.

Rik Bellens (Rik.Bellens@ugent.be) received his Diploma degree in computer science engineering from Ghent University, Belgium, in 2004, where he is currently working toward his Ph.D. degree in the Department of Telecommunications and Information Processing. His main research interests are pattern recognition, remote sensing, image processing, mobility, and crowd behavior. He is a Member of the IEEE.

Sidharta Gautama (Sidharta.Gautama@ugent.be) received his Diploma degree in electrical engineering in 1994 and his Ph.D. degree in applied sciences in 2002, both from Ghent University, Belgium. He currently works in the Department of Telecommunication and Information Processing of Ghent University as a part-time lecturer on

computer vision. He also heads the innovation center i-KNOW at Ghent University, which incubates the licensing and spin-off activity of the research in intelligent information processing. i-KNOW has up to now incorporated four companies and is active in the domains of environment, manufacturing, mobility, and consumer. He is a Member of the IEEE.

Wilfried Philips (Wilfried.Philip@ugent.be) received his Diploma degree in electrical engineering and his Ph.D. degree in applied sciences, both from Ghent University, Belgium, in 1989 and 1993, respectively. He is with the Department of Telecommunications and Information Processing, Ghent University, where he is a full-time professor and head of the research group Image Processing and Interpretation, which is part of the Research Institute Interuniversity MicroElectronics Center. His research interests include image and video restoration, analysis and modeling of image reproduction systems, remote sensing, surveillance, and industrial inspection. He is a Senior Member of the IEEE.

REFERENCES

[1] M. Dalla Mura, S. Prasad, F. Pacifici, P. Gamba, J. Chanussot, and J. Benediktsson, "Challenges and opportunities of multimodality and data fusion in remote sensing," *Proc. IEEE*, vol. 103, no. 9, pp. 1585–1601, Sept. 2015.

[2] C. Debes, A. Merentitis, R. Heremans, J. Hahn, N. Frangiadakis, T. Kasteren, W. Liao, R. Bellens, A. Pizurica, S. Gautama, W. Philips, S. Prasad, Q. Du, and F. Pacifici, "Hyperspectral and LiDAR data fusion: Outcome of the 2013 GRSS data fusion contest," *IEEE J. Sel. Topics Appl. Earth Observ. Remote Sens.*, vol. 7, no. 6, pp. 2405–2418, 2014.

[3] W. Liao, X. Huang, F. Coillie, S. Gautama, A. Pizurica, W. Philips, H. Liu, T. Zhu, M. Shimoni, G. Moser, and D. Tuia, "Processing of multiresolution thermal hyperspectral and digital color data: Outcome of the 2014 IEEE GRSS data fusion contest," *IEEE J. Sel. Topics Appl. Earth Observ. Remote Sens.*, vol. 8, no. 6, pp. 2984–2996, May 2015.

[4] T. Blaschke, "Object based image analysis for remote sensing," *ISPRS J. Photogrammetry Remote Sens.*, vol. 65, no. 1, pp. 2–16, 2010.

[5] S. W. Myint, P. Gober, A. Brazel, S. Grossman-Clarke, and Q. Weng, "Per-pixel vs. object-based classification of urban land cover extraction using high spatial resolution imagery," *Remote Sens. Environ.*, vol. 115, no. 5, pp. 1145–1161, May 2011.

[6] D. C. Duro, S. E. Franklin, and M. G. Dube, "A comparison of pixel-based and object-based image analysis with selected machine learning algorithms for the classification of agricultural landscapes using SPOT-5 HRG imagery," *Remote Sens. Environ.*, vol. 118, no. 6, pp. 259–272, May 2012.

[7] P. Soille, *Morphological Image Analysis, Principles and Applications*, 2nd ed. Berlin: Springer-Verlag, 2003.

[8] M. Pesaresi and J. A. Benediktsson, "A new approach for the morphological segmentation of high-resolution satellite imagery," *IEEE Trans. Geosci. Remote Sens.*, vol. 39, no. 2, pp. 309–320, Feb. 2001.

[9] J. A. Benediktsson, J. Palmason, and J. R. Sveinsson, "Classification of hyperspectral data from urban areas based on extended morphological profiles," *IEEE Trans. Geosci. Remote Sens.*, vol. 43, no. 3, pp. 480–491, Mar. 2005.

[10] R. Bellens, S. Gautama, L. Martinez-Fonte, W. Philips, J. C.-W. Chan, and F. Canters, "Improved classification of VHR images of urban areas using directional morphological profiles," *IEEE Trans. Geosci. Remote Sens.*, vol. 46, no. 10, pp. 2803–2812, Oct. 2008.

[11] M. Dalla Mura, J. A. Benediktsson, B. Waske, and L. Bruzzone, "Morphological attribute profiles for the analysis of very high resolution images," *IEEE Trans. Geosci. Remote Sens.*, vol. 48, no. 10, pp. 3747–3762, Oct. 2010.

[12] M. Dalla Mura, J. A. Benediktsson, B. Waske, and L. Bruzzone, "Extended profiles with morphological attribute filters for the analysis of hyperspectral data," *Int. J. Remote Sens.*, vol. 31, no. 22, pp. 5975–5991, Nov. 2010.

[13] X. Huang and L. Zhang, "Morphological building/shadow index for building extraction from high-resolution imagery over urban areas," *IEEE J. Sel. Topics Appl. Earth Observ. Remote Sens.*, vol. 5, no. 1, pp. 161–172, Feb. 2012.

[14] X. Huang, Q. Lu, and L. Zhang, "A multi-index learning approach for classification of high-resolution remotely sensed images over urban areas," *ISPRS J. Photogrammetry Remote Sens.*, vol. 90, pp. 36–48, Apr. 2014.

[15] X. Huang, H. Liu, and L. Zhang, "Spatiotemporal detection and analysis of urban villages in mega city regions of China using high-resolution remotely sensed imagery," *IEEE Trans. Geosci. Remote Sens.*, vol. 53, no. 7, pp. 3639–3657, Jan. 2015.

[16] L. Bruzzone and F. Bovolo, "A novel framework for the design of change-detection systems for very-high-resolution remote sensing images," *Proc. IEEE*, vol. 101, no. 3, pp. 609–630, 2013.

[17] K. Zhang, "Identification of gaps in mangrove forests with airborne LIDAR," *Remote Sens. Environ.*, vol. 112, no. 5, pp. 2309–2335, May 2008.

[18] A. C. Braun, C. Rojas, C. Echeverri, F. Rottensteiner, H. P. Bahr, J. Niemeyer, M. Aguayo Arias, S. Kosov, S. Hinz, and U. Weidner, "Design of a spectral-spatial pattern recognition framework for risk assessments using Landsat dataork for risk assessment," *IEEE J. Sel. Topics Appl. Earth Observ. Remote Sens.*, vol. 7, no. 3, pp. 917–928, 2014.

[19] D. Mongus and B. Zalik, "Computationally efficient method for the generation of a digital terrain model from airborne LiDAR data using connected operators," *IEEE J. Sel. Topics Appl. Earth Observ. Remote Sens.*, vol. 7, no. 1, pp. 340–351, May 2013.

[20] W. Liao, R. Bellens, A. Pizurica, S. Gautama, and W. Philips, "Generalized graph-based fusion of hyperspectral and LiDAR data using morphological features," *IEEE Geosci. Remote Sens. Lett.*, vol. 12, no. 3, pp. 552–556, Mar. 2015.

[21] J. M. Daida and J. F. Vesecky, "Mathematical morphology for automated analysis of remotely sensed objects in radar images," in *Proc. 1991 IEEE Geoscience and Remote Sensing Symp.*, Espoo, Finland, 1991, vol. 3, pp. 1795–1799.

[22] G. Laneve, G. Santilli, and E. Cadau, "Application of mathematical morphology to automatically extract roads on radar images," in *Proc. Joint Urban Remote Sensing Event*, Shanghai, China, May 2009, pp. 1–5.

[23] A. Gasull, X. Fabregas, J. Jimenez, F. Marques, V. Moreno, and M. Herrero, "Oil spills detection in SAR images using mathematical morphology," *Proc. European Signal Processing Conf.* Toulouse, France, Sept. 2002, vol. 1, pp. 25–28.

[24] A. Plaza, J. Benediktsson, J. Boardman, J. Brazile, L. Bruzzone, G. Camps-Valls, J. Chanussot, M. Fauvel, P. Gamba, A. Gualtieri, M. Marconcini, J. C. Tilton, and G. Trianni, "Recent advances in techniques for hyperspectral image processing," *Remote Sens. Environ.*, vol. 113, pp. S110–S122, Sept. 2009.

[25] T. Castaings, B. Waske, J. A. Benediktsson, and J. Chanussot, "On the influence of feature reduction for the classification of hyperspectral images based on the extended morphological profile," *Int. J. Remote Sens.*, vol. 31, no. 22, pp. 5921–5939, July 2010.

[26] M. Fauvel, Y. Tarabalka, J. Benediktsson, J. Chanussot, and J. C. Tilton, "Advances in spectral-spatial classification of hyperspectral Images, *Proc. IEEE*, vol. 101, no. 3, pp. 652–675, Sept. 2012.

[27] R. M. Haralick, S. Sternberg, and X. Zhuang, "Image analysis using mathematical morphology," *IEEE Trans. Pattern Anal. Mach. Intell.*, vol. PAMI 9, no. 4, pp. 532–550, July 1987.

[28] S. Morales, V. Naranjo, J. Angulo, and M. Alcaniz, "Automatic detection of optic disc based on PCA and mathematical morphology," *IEEE Trans. Med. Imag.*, vol. 32, no. 4, pp. 786–796, Jan. 2013.

[29] B. Perret, J. Cousty, O. Tankyevych, H. Talbot, and N. Passat, "Directed connected operators: Asymmetric hierarchies for image filtering and segmentation," *IEEE Trans. Pattern Anal. Mach. Intell.*, vol. 37, no. 6, pp. 1162–1176, Oct. 2014.

[30] P. M. Neila, L. Baumela, and L. Alvarez, "A morphological approach to curvature-based evolution of curves and surfaces," *IEEE Trans. Pattern Anal. Mach. Intell.*, vol. 36, no. 1, pp. 2–17, June 2013.

[31] P. Ghamisi, M. Dalla Mura, and J. A. Benediktsson, "A survey on spectral-spatial classification techniques based on attribute profiles," *IEEE Trans. Geosci. Remote Sens.*, vol. 53, no. 5, pp. 2335–2353, May 2015.

[32] M. Dalla Mura, A. Villa, J. A. Benediktsson, J. Chanussot, and L. Bruzzone, "Classification of hyperspectral images by using extended morphological attribute profiles and independent component analysis," *IEEE Geosci. Remote Sens. Lett.*, vol. 8, no. 3, pp. 541–545, May 2011.

[33] M. Khodadadzadeh, J. Li, S. Prasad, and A. Plaza, "Fusion of hyperspectral and LiDAR remote sensing data using multiple feature learning," *IEEE J. Sel. Topics Appl. Earth Observ. Remote Sens.*, vol. 8, no. 6, pp. 2971–2983, June 2015.

[34] W. Liao, M. Dalla Mura, X. Huang, J. Chanussot, S. Gautama, P. Scheunders, and W. Philips, "Lidar information extraction by attribute filters with partial reconstruction," in *Proc. 2016 IEEE Geoscience Remote Sensing Int. Symp.*, Beijing, China, July 2016, pp. 1484–1487.

[35] P. R. Marpu, K. Chen, C. Chu, and J. Benediktsson, "Spectral-spatial classification of polarimetric SAR data using morphological profiles," in *Proc. 3rd Int. Asia-Pacific Conf. Synthetic Aperture Radar*, Seoul, South Korea, 2011, pp. 1–3.

[36] R. Restaino, G. Vivone, M. Dalla Mura, and J. Chanussot, "Fusion of multispectral and panchromatic images based on

morphological operators," *IEEE Trans. Image Process.*, vol. 25, no. 6, pp. 2882–2895, June 2016.

[37] B. Demir and L. Bruzzone, "Histogram-based attribute profiles for classification of very high resolution remote sensing images," *IEEE Trans. Geosci. Remote Sens.*, vol. 54, no. 4, pp. 2096–2107, Apr. 2016.

[38] M. Pedergnana, P. Reddy Marpu, M. Dalla Mura, J. A. Benediktsson, and L. Bruzzone, "Classification of remote sensing optical and LiDAR data using extended attribute profiles," *IEEE J. Sel. Topics Signal Process.*, vol. 6, no. 7, pp. 856–865, Nov. 2012.

[39] M. Pedergnana, P. R. Marpu, M. Dalla Mura, J. A. Benediktsson, and L. Bruzzone, "A Novel technique for optimal feature selection in attribute profiles based on genetic algorithms," *IEEE Trans. Geosci. Remote Sens.*, vol. 51, no. 6, pp. 3514–3528, June 2013.

[40] P. Ghamisi, J. A. Benediktsson, and J. R. Sveinsson, "Automatic spectral-spatial classification framework based on attribute profiles and supervised feature extraction," *IEEE Trans. Geosci. Remote Sens.*, vol. 52, no. 9, pp. 5771–5782, May 2014.

[41] B. Song, J. Li, M. Dalla Mura, P. Li, A. Plaza, J. M. Bioucas Dias, J. A. Benediktsson, and J. Chanussot, "Remotely sensed image classification using sparse representations of morphological attribute profiles," *IEEE Trans. Geosci. Remote Sensing*, vol. 52, no. 8, pp. 5122–5136, Aug. 2014.

[42] J. Li, X. Huang, P. Gamba, J. Bioucas, L. Zhang, J. A. Benediktsson, and A. Plaza, "Multiple feature learning for hyperspectral image classification," *IEEE Trans. Geosci. Remote Sens.*, vol. 53, no. 3, pp. 1592–1606, Mar. 2015.

[43] J. Xia, M. Dalla Mura, J. Chanussot, P. Du, and X. He, "Random subspace ensembles for hyperspectral image classification with extended morphological attribute profiles," *IEEE Trans. Geosci. Remote Sens.*, vol. 53, no. 9, pp. 4768–4786, Mar. 2015.

[44] G. Cavallaro, M. Dalla Mura, and J. Benediktsson, "Processing high resolution images of urban areas with self-dual attribute filters," in *Proc. 2015 Joint Urban Remote Sensing Event*, Lausanne, Switzerland, March 2015, pp. 1–4.

[45] C. Ronse, "Set-theoretical algebraic approaches to connectivity in continuous or digital spaces," *J. Math. Imag. Vision*, vol. 8, no. 1, pp. 41–58, 1998.

[46] G. K. Ouzounis and M. H. F. Wilkinson, "Mask-based second generation connectivity and attribute filters," *IEEE Trans. Pattern Anal. Mach. Intell.*, vol. 29, no. 6, pp. 990–1004, 2007.

[47] M. H. F. Wilkinson, "Connected filtering by reconstruction: Basis and new advances," in *Proc. 15th IEEE Int. Conf. Image Processing*, San Diego, California, Oct. 2008, pp. 2180–2183.

[48] P. Salembier and M. H. F. Wilkinson, "Connected operators," *IEEE Signal Processing Mag.*, vol. 26, no. 6, pp. 136–157, Nov. 2009.

[49] L. Vincent, "Morphological grayscale reconstruction: Definition, efficient algorithm and applications in image analysis," in *Proc. IEEE Conf. Comp. Vision and Pattern Recog.*, Champaign, IL, June 1992, pp. 633–635.

[50] L. Vincent, "Morphological grayscale reconstruction in image analysis: Applications and efficient algorithms," *IEEE Trans. Image Process.*, vol. 2, no. 2, pp. 176–201, Feb. 1993.

[51] W. Liao, M. Dalla Mura, J. Chanussot, R. Bellens, and W. Philips, "Morphological attribute profiles with partial reconstruction," *IEEE Trans. Geosci. Remote Sens.*, vol. 54, no. 3, pp. 1738–1756, 2016.

[52] G. K. Ouzounis and M. H. F. Wilkinson, "Partition-induced connections and operators for pattern analysis," *Pattern Recognition*, vol. 43, no. 10, pp. 3193–3207, 2010.

[53] W. Liao, R. Bellens, A. Pižurica, W. Philips, and Y. Pi, "Classification of hyperspectral data over urban areas using directional morphological profiles and semi-supervised feature extraction," *IEEE J. Sel. Topics Appl. Earth Observ. Remote Sens.*, vol. 5, no. 4, pp. 1177–1190, Aug. 2012.

[54] W. Liao, R. Bellens, A. Pižurica, W. Philips, and Y. Pi, "Classification of hyperspectral data over urban areas based on extended morphological profile with partial reconstruction," in *Proc. Advanced Concepts for Intelligent Vision Systems*, Brno, Czech Republic, 2012, pp. 278–289, 2012.

[55] IEEE GRSS. (2013). Image analysis and data fusion. [Online]. Available: http://www.grss-ieee.org/community/technical-committees/data-fusion/

[56] J. Crespo, J. Serra, and R. Shafer, "Theoretical aspects of morphological filters by reconstruction," *Signal Process.*, vol. 47, no. 2, pp. 201–225, Nov. 1995.

[57] M. Fauvel, J. A. Benediktsson, J. Chanussot, and J. R. Sveinsson, "Spectral and spatial classification of hyperspectral data using SVMs and morphological profile," *IEEE Trans. Geosci. Remote Sens.*, vol. 46, no. 11, pp. 3804–3814, Nov. 2008.

[58] E. J. Breen and R. Jones, "Attribute openings, thinnings and granulometries," *Comput. Vision Image Understanding*, vol. 64, no. 3, pp. 377–389, Nov. 1996.

[59] C. J. C. Burges, "A tutorial on support vector machines for pattern recognition," *Data Mining Knowledge Discovery*, vol. 2, pp. 121–167, 1998.

[60] G. F. Hughes, "On the mean accuracy of statistical pattern recognizers," *IEEE Trans. Inf. Theory*, vol. 14, no. 1, pp. 55–63, 1968.

[61] C. C. Chang and C. J. Lin. (2001). LIBSVM: A library for support vector machines. [Online]. Available: http://www.csie.ntu.edu.tw/~cjlin/libsvm

[62] A. Plaza, P. Martinez, J. Plaza, and R. M. Perez, "Dimensionality reduction and classification of hyperspectral image data using sequences of extended morphological transformations," *IEEE Trans. Geosci. Remote Sens.*, vol. 43, no. 3, pp. 466–479, Mar. 2005.

[63] M. Fauvel, J. Chanussot, and J. A. Benediktsson, "Kernel principal component analysis for the classification of hyperspectral remote-sensing data over urban areas," in *Proc. EURASIP J. Advances Signal Process.*, vol. 2009, p. 14, Feb. 2009, pp. 1–14.

[64] J. A. Richards and X. Jia, *Remote Sensing Digital Image Analysis: An Introduction*. New York: Springer, 1999.

[65] Z. Mahmood, G. Thoonen, and P. Scheunders, "Automatic threshold selection for morphological attribute profiles," in *Proc. Int. Geoscience and Remote Sensing Symp.*, Munich, July 2012, pp. 4946–4949.

GRS